

Parameterization of the Bulk Liquid Fraction on Mixed-Phase Particles in the Predicted Particle Properties (P3) Scheme: Description and Idealized Simulations

MÉLISSA CHOLETTE

Centre pour l'Étude et la Simulation du Climat à l'Échelle Régionale, Department of Earth and Atmospheric Sciences, Université du Québec à Montréal, Montreal, Quebec, Canada

HUGH MORRISON

National Center for Atmospheric Research, Boulder, Colorado

JASON A. MILBRANDT

Atmospheric Numerical Prediction Research, Environment and Climate Change Canada, Dorval, Quebec, Canada

JULIE M. THÉRIAULT

Centre pour l'Étude et la Simulation du Climat à l'Échelle Régionale, Department of Earth and Atmospheric Sciences, Université du Québec à Montréal, Montreal, Quebec, Canada

(Manuscript received 12 September 2018, in final form 14 November 2018)

ABSTRACT

Bulk microphysics parameterizations that are used to represent clouds and precipitation usually allow only solid and liquid hydrometeors. Predicting the bulk liquid fraction on ice allows an explicit representation of mixed-phase particles and various precipitation types, such as wet snow and ice pellets. In this paper, an approach for the representation of the bulk liquid fraction into the predicted particle properties (P3) microphysics scheme is proposed and described. Solid-phase microphysical processes, such as melting and sublimation, have been modified to account for the liquid component. New processes, such as refreezing and condensation of the liquid portion of mixed-phase particles, have been added to the parameterization. Idealized simulations using a one-dimensional framework illustrate the overall behavior of the modified scheme. The proposed approach compares well to a Lagrangian benchmark model. Temperatures required for populations of ice crystals to melt completely also agree well with previous studies. The new processes of refreezing and condensation impact both the surface precipitation type and feedback between the temperature and the phase changes. Overall, prediction of the bulk liquid fraction allows an explicit description of new precipitation types, such as wet snow and ice pellets, and improves the representation of hydrometeor properties when the temperature is near 0°C.

1. Introduction

The passage of a warm front can produce favorable environmental conditions for many winter precipitation types such as rain, freezing rain, ice pellets, wet snow, and snow (Stewart 1985). In such situations, a temperature (T) inversion, characterized by a warm layer aloft

with $T > 0^{\circ}\text{C}$ (called the melting layer) and cold layer near the surface with $T < 0^{\circ}\text{C}$ (called the refreezing layer), occurs (e.g., Carmichael et al. 2011; Thériault et al. 2006; Gyakum and Roebber 2001; Hanesiak and Stewart 1995; Lin and Stewart 1986). The precipitation types formed when the temperature is near 0°C involve several microphysical processes including melting, refreezing, vapor deposition, collection, and wet growth. For example, when $T > \sim 0^{\circ}\text{C}$, wet snow is formed from the partial melting of snow during which the melted water tends to accumulate on the ice core to form mixed-phase particles (Fujiyoshi 1986). Ice pellets are formed by refreezing in cold layers of the partially melted

 Denotes content that is immediately available upon publication as open access.

Corresponding author: Mélissa Cholette, cholette.melissa@courrier.uqam.ca

DOI: 10.1175/JAS-D-18-0278.1

© 2019 American Meteorological Society. For information regarding reuse of this content and general copyright information, consult the [AMS Copyright Policy \(www.ametsoc.org/PUBSReuseLicenses\)](#).

particles from aloft (Carmichael et al. 2011; Thériault and Stewart 2010; Gibson and Stewart 2007). Freezing rain corresponds to the surface icing of supercooled raindrops present in cold layers originating from the total melting of snow in warm layers aloft. Often, several types of precipitation can coexist, and, for example, the amount of surface freezing rain can be greatly inhibited because of the collection in the cold layers between supercooled raindrops and solid hydrometeors, such as ice pellets (Barszcz 2017; Carmichael et al. 2011; Hogan 1985). When $T < 0^{\circ}\text{C}$, wet growth of graupel/hail and the shedding of accumulated liquid water can occur in conditions of high liquid water content, also involving the formation of mixed-phase particles (e.g., Phillips et al. 2014). In turn, the phase changes occurring with some of these processes impact the environmental temperature as, for example, the cooling induced by melting and evaporation (e.g., Lackmann et al. 2002) or the warming induced by refreezing and condensation (e.g., Thériault et al. 2006).

Most bulk microphysics schemes allow only for the representation of solid-phase hydrometeors (e.g., snow, graupel, hail) and liquid-phase hydrometeors (e.g., rain, cloud) (e.g., Morrison et al. 2009; Thompson et al. 2008; Milbrandt and Yau 2005). Mixed-phase hydrometeors, such as wet snow, are typically not represented. For example, instead of forming wet snow from partial melting, most schemes immediately transfer the melted water directly into the rain category. To represent the evolution of mixed-phase particles in microphysical parameterizations explicitly, it is necessary to track in space and time the liquid fraction of mixed-phase hydrometeors, defined as the ratio of liquid water mass to the total particle mass.

Some studies have experimented with an explicit parameterization of the liquid fraction. Based on the experimental and theoretical relationships developed by Mitra et al. (1990, hereafter M90), the study of Szyrmer and Zawadzki (1999) predicted the liquid fraction in a bulk microphysics module. This scheme was coupled with a two-dimensional nonhydrostatic, fully compressible dynamic framework to evaluate the effects of partial melting on the simulated “brightband” parameters (Fabry and Szyrmer 1999; Braun and Houze 1995; Fabry and Zawadzki 1995; Yokoyama and Tanaka 1984; Austin and Bemis 1950). They showed that the description of the particle habit prior to melting (unrimed or rimed and spherical or nonspherical) influences the melting rate and the liquid fraction evolution. They also pointed out the relevance of predicting the liquid fraction for radar applications. Based on the Szyrmer and Zawadzki (1999) parameterization, Thériault and Stewart (2010) modified the Milbrandt and Yau (2005) scheme to include several winter precipitation type categories. The new categories were wet snow, almost

completely melted snow, refrozen wet snow, and two types of ice pellets. They tested the scheme using a one-dimensional (1D) cloud model and showed good agreement with observations for several winter storms (Thériault and Stewart 2010; Thériault et al. 2010, 2006). More recently, and also based on Szyrmer and Zawadzki (1999), Frick et al. (2013) implemented partial melting in a bulk microphysics scheme coupled with the Consortium for Small-Scale Modeling (COSMO; Doms and Schättler 2002) mesoscale model. They clearly showed the potential of their parameterization to simulate wet snow; however, their parameterization did not include the refreezing process, which is necessary to produce ice pellets. The implementation of an explicit liquid fraction has also been tested using bin microphysics parameterizations (Reeves et al. 2016; Geresdi et al. 2014; Phillips et al. 2007). Walko et al. (2000) developed an algorithm to diagnose the liquid fraction in the Regional Atmospheric Modeling System, which can be used with larger numerical time steps and regional modeling.

Recently, the predicted particle properties (P3) bulk microphysics scheme described in Morrison and Milbrandt (2015, hereafter MM15) and Milbrandt and Morrison (2016, hereafter MM16) was introduced. The P3 scheme completely abandons the use of predefined ice-phase categories and introduces the idea of “free” ice categories. With four prognostic variables per free category, important physical properties of ice can evolve realistically and smoothly in time and space, and thus, a wide range of ice particle types can be represented. Despite the conceptual improvement over traditional fixed-category schemes for representing ice, P3 is still limited in that it cannot represent ice particles that accumulate liquid water. To address this limitation, in this study, the original P3 scheme is modified to include the prediction of the bulk liquid fraction of ice categories and thus allow the representation of mixed-phase particles.

This paper is organized as follows. Section 2 briefly describes the original P3 scheme. Section 3 describes the implementation of the bulk liquid fraction into P3. Section 4 shows a validation of the proposed melting parameterization compared to a Lagrangian benchmark model. Section 5 shows results from two idealized experiments using a one-dimensional modeling framework to illustrate the overall behavior of the new parameterization and compare with the original one. Section 6 gives concluding remarks.

2. Overview of the original P3 microphysics scheme

This section gives a brief overview of the original P3 microphysics scheme (referred to as P3_ORIG); further

details are in MM15 and MM16. As in other bulk schemes, P3 has two liquid-phase categories, cloud and rain, both of which are two moment, with prognostic mass and number mixing ratios for each. There is a user-specified number of free ice-phase categories, each with four prognostic variables. In this study, only the single-ice category configuration is discussed, but the modifications described below are general and can apply to multi-ice category configurations. The four prognostic ice variables are total ice mass $q_{i,tot}$ (kg kg^{-1}), total ice number $N_{i,tot}$ (kg^{-1}), rime mass $q_{i,rim}$ (kg kg^{-1}), and rime volume $B_{i,rim}$ ($\text{m}^3 \text{kg}^{-1}$) mixing ratios. One can calculate the vapor deposition ice mass $q_{i,dep}$ from $q_{i,tot}$ minus $q_{i,rim}$. Several relevant bulk properties, including the rime mass fraction ($F_{i,rim} = q_{i,rim}/q_{i,tot}$), the bulk ice density, the bulk rime density ($\rho_{i,rim} = q_{i,rim}/B_{i,rim}$), the mean particle size, and the mean number- and mass-weighted fall speeds are derived from these four conserved prognostic variables.

The total number and ice mass mixing ratios are, respectively, given by

$$N_{i,tot} = \int_0^\infty N_0 D^\mu \exp(-\lambda D) dD, \tag{1}$$

$$q_{i,tot} = \int_0^\infty m_d(D) N_0 D^\mu \exp(-\lambda D) dD, \tag{2}$$

where D is the maximum dimension of the ice particles, $m_d(D)$ is the mass–dimension relationship, and the particle size distribution (PSD) is assumed to follow a gamma function (all symbols for variables and parameters used in the paper are defined in Table 1). The gamma distribution is described by N_0 , λ , and μ , respectively, being the intercept, slope, and shape parameters. In P3, the shape parameter follows from the observational study of Heymsfield (2003): $\mu = 0.00191\lambda^{0.8} - 2$, where λ has units of per meter. For a given combination of prognostic variables ($N_{i,tot}$, $q_{i,tot}$), to solve for the PSD intercept and slope parameters, the $m_d(D)$ is needed.

Similar to Morrison and Grabowski (2008), the $m_d(D)$ follows specific power laws for various size-dependent regimes (see MM15 for details):

$$m_d(D) = \begin{cases} \frac{\pi}{6} \rho_i D^3 & \text{if } D \leq D_{th}: \text{small spherical ice particles} & (3a) \\ \alpha_{va} D^{\beta_{va}} & \text{if } D_{th} < D \leq D_{gr}: \text{unrimed nonspherical ice} & (3b) \\ \frac{\pi}{6} \rho_g D^3 & \text{if } D_{gr} < D \leq D_{cr}: \text{graupel/hail particles} & (3c) \\ \frac{\alpha_{va} (1 + F_{i,rim})}{1 - F_{i,rim}} D^{\beta_{va}} & \text{if } D > D_{cr}: \text{partially rimed nonspherical ice,} & (3d) \end{cases}$$

where $\rho_i = 917 \text{ kg m}^{-3}$ is the density of bulk ice and ρ_g is the density of fully rimed ice (graupel/hail). The regimes are bounded by three threshold diameters,

$$D_{th} = \left(\frac{\pi \rho_i}{6 \alpha_{va}} \right)^{1/\beta_{va} - 3}, \tag{4a}$$

$$D_{gr} = \left(\frac{6 \alpha_{va}}{\pi \rho_g} \right)^{1/3 - \beta_{va}}, \tag{4b}$$

$$D_{cr} = \left[\frac{6 \alpha_{va} (1 + F_{i,rim})}{\pi \rho_g (1 - F_{i,rim})} \right]^{1/\beta_{va}}, \tag{4c}$$

that can evolve within the PSD as a function of the ice regime. The parameters α_{va} and β_{va} are empirical constants, and herein, we use default P3 values of $\alpha_{va} = 0.0121 \text{ kg m}^{-\beta_{va}}$ and $\beta_{va} = 1.9$ following Brown and

Francis (1995), modified for the correction proposed by Hogan et al. (2012). Diameter D_{th} in (4a) smoothly divides small spherical ice particles from unrimed nonspherical particles and is found by equating (3a) and (3b). This threshold is needed because extrapolation of the $m_d(D)$ relationship for unrimed nonspherical ice to sizes smaller than D_{th} would give particle densities larger than ρ_i , which is unphysical. Diameter D_{gr} , given by (4b), smoothly separates dense, unrimed, nonspherical ice particles from graupel/hail and is found by equating (3b) and (3c). This is the size at which the masses of a completely rime-filled particle (graupel/hail) and of an unrimed nonspherical ice particle are equal for a given diameter D . Finally, D_{cr} in (4c) smoothly divides graupel/hail from partially rimed nonspherical ice and is obtained by equating (3c) and (3d). Physically, this threshold originates directly from the assumption that the rime mass fraction does not vary with D , giving a

TABLE 1. List of symbols for variables and parameters.

Symbol	Description	Units
$A_d(D)$	Projected area– D relationship for ice particles in P3_ORIG	m^2
$A_d(D_x)$	Projected area– D_x relationship for mixed-phase particles; D_x can be D_p or D_d	m^2
$A_{i,\text{wet}}$	Forcing term for supersaturation due to vertical motion	$\text{kg kg}^{-1} \text{s}^{-1}$
$A_{\text{liq}}(D_p)$	Projected area– D_p for liquid drops ($F_{i,\text{liq}} = 1$)	m^2
$A_i(D_p, F_{i,\text{liq}})$	Projected area relationship of the whole particle in P3_MOD	m^2
α_{va}	Coefficient for unrimed nonspherical ice particle mass	$\text{kg m}^{-\beta_{\text{va}}}$
$B_{i,\text{rim}}$	Rime volume mixing ratio of ice	$\text{m}^3 \text{kg}^{-1}$
β_{va}	Coefficient for unrimed nonspherical ice particle mass	—
$C(D_d, F_{i,\text{liq}})$	Capacitance for melting of the ice core of mixed-phase particles	m
$C_d(D_x)$	Capacitance for dry ice ($F_{i,\text{liq}} = 0$); D_x can be D_p or D_d	m
$C(D_p, F_{i,\text{liq}})$	Capacitance for condensation/evaporation and refreezing of mixed-phase particles	m
$C_{\text{liq}}(D_x)$	Capacitance for liquid drops ($F_{i,\text{liq}} = 1$); D_x can be D_p or D_d	m
D	Maximum dimension of ice particles in P3_ORIG	m
D_{cr}	Threshold diameter separating graupel/hail from partially rimed nonspherical ice particles	m
D_d	Maximum dimension of the ice core of mixed-phase particles	m
D_{eq}	Spherical drop equivalent diameter	m
D_{gr}	Threshold diameter separating unrimed nonspherical ice particles from graupel/hail	m
$\frac{dm_{\text{ice}}}{dt} \Big _{\text{melting}}$	The mass melting rate of a particle	kg s^{-1}
$\frac{dm_{\text{tot}}}{dt} \Big _{\text{freezing}}$	The mass refreezing rate of a particle	kg s^{-1}
D_p	Dimension of mixed-phase particles	m
D_{th}	Threshold diameter separating small spherical ice particles from unrimed nonspherical ice particles	m
D_v	Diffusivity of water vapor in air	$\text{m}^2 \text{s}^{-1}$
D^*	Melting critical diameter	m
$F(D_d, F_{i,\text{liq}})$	Ventilation factor for melting of ice cores in mixed-phase particles	—
$F_d(D_d)$	Ventilation factor for dry ice ($F_{i,\text{liq}} = 0$)	—
$F(D_p, F_{i,\text{liq}})$	Ventilation factor for whole mixed-phase particles	—
$F_{i,\text{liq}}$	Bulk liquid mass fraction	—
$F_{i,\text{rim}}$	Bulk rime mass fraction	—
$F_{\text{liq}}(D_d)$	Ventilation factor for liquid drops ($F_{i,\text{liq}} = 1$)	—
g	Gravitational acceleration	m s^{-2}
Γ_l	Psychrometric correction associated with the latent heating/cooling	—
k_a	Thermal conductivity of air	—
L_e, L_f, L_s	Latent heats of evaporation, fusion, and sublimation, respectively	$\text{J K}^{-1} \text{kg}^{-1}$
$m_d(D)$	Mass– D relationship of ice particles in P3_ORIG	kg
$m_d(D_x)$	Mass– D_x relationship of the ice-core component of mixed-phase particles; D_x can be D_p or D_d	kg
$m_{\text{liq}}(D_p)$	Mass– D_p relationship for liquid drops ($F_{i,\text{liq}} = 1$)	kg
$m_i(D_p, F_{i,\text{liq}})$	Mass– D_p relationship of whole mixed-phase particles	kg
$N_{i,\text{tot}}$	Total ice number mixing ratio	kg^{-1}
$N_{l,\text{evp}}$	$N_{i,\text{tot}}$ sink term of evaporation of $q_{i,\text{liq}}$	$\text{kg}^{-1} \text{s}^{-1}$
$N_0, N_{0,\text{core}}, N_{0,p}$	PSD intercept parameter in P3_ORIG, for ice cores in P3_MOD and for whole particles in P3_MOD, respectively	$\text{kg}^{-1} \text{m}^{-(1+\mu)}$
N_{rain}	Rain number mixing ratio	kg^{-1}
$N_{r,\text{melt}}$	$N_{i,\text{tot}}$ (N_{rain}) sink (source) term of melting	$\text{kg}^{-1} \text{s}^{-1}$
ρ	Mass-weighted mean particle density	kg m^{-3}
ρ_a	Air density	kg m^{-3}
ρ_i	Density of solid ice	kg m^{-3}
$\rho_{i,\text{rim}}$	Rime density	kg m^{-3}
ρ_g	Graupel/hail density	kg m^{-3}
ρ_{ur}	Density of the unrimed component of ice particles between D_{gr} and D_{cr}	kg m^{-3}
ρ_w ($\rho_{w,g}$)	Liquid water density	kg m^{-3} (g m^{-3})
$q_{i,\text{dep}}$	Vapor deposition mass mixing ratio	kg kg^{-1}
$q_{i,\text{ice}}$	Ice mass mixing ratio	kg kg^{-1}
$q_{i,\text{liq}}$	Liquid mass mixing ratio accumulated on ice	kg kg^{-1}
$Q_{i,\text{melt}}$	$q_{i,\text{liq}}$ source term of melting	$\text{kg kg}^{-1} \text{s}^{-1}$
$q_{i,\text{rim}}$	Rime mass mixing ratio	kg kg^{-1}

TABLE 1. (Continued)

Symbol	Description	Units
$q_{i,tot}$	Total mass mixing ratio of ice and mixed-phase particles	kg kg^{-1}
$Q_{i,coll,c}$	$q_{i,liq}$ source term of collection with cloud droplets	$\text{kg kg}^{-1} \text{s}^{-1}$
$Q_{i,coll,r}$	$q_{i,liq}$ source term of collection with raindrops	$\text{kg kg}^{-1} \text{s}^{-1}$
$Q_{i,dep}$	$q_{i,liq}$ source/sink term of vapor transfer	$\text{kg kg}^{-1} \text{s}^{-1}$
$Q_{i,frz}$	$q_{i,liq}$ sink term of refreezing	$\text{kg kg}^{-1} \text{s}^{-1}$
$Q_{i,shd}$	$q_{i,liq}$ sink term of shedding	$\text{kg kg}^{-1} \text{s}^{-1}$
$Q_{i,wgrth}$	$q_{i,liq}$ source term of wet growth	$\text{kg kg}^{-1} \text{s}^{-1}$
q_{rain}	Rain mass mixing ratio	kg kg^{-1}
$Q_{r,mlt}$	q_{rain} source term of melting	$\text{kg kg}^{-1} \text{s}^{-1}$
$q_{s,0}$	Saturated water vapor mixing ratio	kg kg^{-1}
q_v	Water vapor mixing ratio	kg kg^{-1}
Re, Re_d, Re_r	Reynolds number for calculating $F(D_p, F_{i,liq}), F_d(D_d)$, and $F_{liq}(D_d)$, respectively	—
Sc	Schmidt number	—
$\delta_{t=0}$	Supersaturation at the beginning of the time step	kg kg^{-1}
Δt	Time step	s
t	Time	min
T	Air temperature	$^{\circ}\text{C}$
T_0	Freezing point (0°C)	$^{\circ}\text{C}$
T_d	Dewpoint temperature	$^{\circ}\text{C}$
$\tau_c, \tau_{i,wet}, \tau_r, \tau$	Relaxation time scale of cloud, wet ice, rain, and total ice for evaporation/condensation in P3_MOD, respectively	—
\mathbf{u}	3D wind vector	—
μ, μ_{core}, μ_p	PSD shape parameter in P3_ORIG, for ice cores in P3_MOD and for whole particles in P3_MOD, respectively	—
ν	Dynamic viscosity of air	Pa s^{-1}
V_m, V_N	Mass- and number-weighted mean fall speeds, respectively	m s^{-1}
$V_t(D)$	Terminal velocity– D relationship of P3_ORIG	m s^{-1}
$V_t(D_p, F_{i,liq})$	Terminal velocity relationship of P3_MOD	m s^{-1}
$V_t(D_x, F_{i,liq} = 0)$	Terminal velocity relationship when $F_{i,liq} = 0$; D_x can be D_d or D_p	m s^{-1}
$V_t(D_x, F_{i,liq} = 1)$	Terminal velocity relationship when $F_{i,liq} = 1$; D_x can be D_d or D_p	m s^{-1}
X_p, X_d, X_r	Best numbers for calculating $F(D_p, F_{i,liq}), F_d(D_d)$, and $F_{liq}(D_d)$, respectively	—
$\lambda, \lambda_{core}, \lambda_p$	PSD slope parameter in P3_ORIG, for ice cores in P3_MOD and for whole particles in P3_MOD, respectively	m^{-1}
z	Height	km

critical size D_{cr} below which particles are completely filled in with rime.

The value of ρ_g is an $F_{i,rim}$ -weighted average of the rime density $\rho_{i,rim}$ and the density underlying the unrimed structure of the particle ρ_{ur} (see MM15 for details). Because of their complicated interrelationship, the equations for D_{gr} , D_{cr} , ρ_g , and ρ_{ur} are solved together by iteration (MM15; Dietlicher et al. 2018). The projected area–diameter relationship $A_d(D)$ also follows specific power laws for various size-dependent regimes consistent with the $m_d(D)$ relationship (MM15). The terminal velocity–diameter relationship $V_t(D)$ is computed using $m_d(D)$ and $A_d(D)$ according to Mitchell and Heymsfield (2005).

Once the parameters for the PSD (N_0 , λ , and μ) and the $m_d(D)$, $A_d(D)$, and $V_t(D)$ relationships are obtained, all the microphysical process rates are integrated. This is done offline, and the

values are stored in lookup tables as a function of the normalized total ice mass $q_{i,tot}/N_{i,tot}$, the bulk rime density $\rho_{i,rim}$, and the bulk rime mass fraction $F_{i,rim}$.

3. Parameterization description of the bulk liquid fraction

a. Overview of the liquid mass mixing ratio

To simulate mixed-phase particles and $F_{i,liq}$ explicitly in P3, a new conserved prognostic variable, the liquid mass mixing ratio on ice particles $q_{i,liq}$, has been added to P3_ORIG. The modified scheme will be referred to as P3_MOD. In P3_MOD,

$$q_{i,tot} = q_{i,ice} + q_{i,liq} = q_{i,rim} + q_{i,dep} + q_{i,liq}, \quad (5)$$

where $q_{i,ice} = q_{i,rim} + q_{i,dep}$. The bulk rime mass and liquid mass fractions are thus defined by

$$F_{i,\text{rim}} = \frac{q_{i,\text{rim}}}{q_{i,\text{ice}}} = \frac{q_{i,\text{rim}}}{q_{i,\text{rim}} + q_{i,\text{dep}}}, \quad (6)$$

$$F_{i,\text{liq}} = \frac{q_{i,\text{liq}}}{q_{i,\text{tot}}} = \frac{q_{i,\text{liq}}}{q_{i,\text{rim}} + q_{i,\text{dep}} + q_{i,\text{liq}}}, \quad (7)$$

respectively. The conservation equation for $q_{i,\text{liq}}$ is

$$\frac{\partial q_{i,\text{liq}}}{\partial t} = -\mathbf{u} \cdot \nabla q_{i,\text{liq}} + \frac{1}{\rho_a} \frac{\partial(\rho_a V_m q_{i,\text{liq}})}{\partial z} + \Delta^*(q_{i,\text{liq}}) + \left. \frac{dq_{i,\text{liq}}}{dt} \right|_S, \quad (8)$$

where t is time, ρ_a is the air density, \mathbf{u} is the 3D wind vector, z is height, V_m is the mass-weighted fall speed (see appendix A), $\Delta^*(q_{i,\text{liq}})$ is a subgrid-scale mixing operator, and $(dq_{i,\text{liq}}/dt)|_S$ is a source–sink term that includes various microphysical processes. The $q_{i,\text{liq}}$ microphysical tendency is

$$\left. \frac{dq_{i,\text{liq}}}{dt} \right|_S = Q_{i,\text{melt}} + Q_{i,\text{wgrth}} + Q_{i,\text{coll},r} + Q_{i,\text{coll},c} + Q_{i,\text{dep}} - Q_{i,\text{frz}} - Q_{i,\text{shd}}, \quad (9)$$

where $Q_{i,\text{melt}}$ is the melting, $Q_{i,\text{wgrth}}$ the wet growth, $Q_{i,\text{coll},r}$ ($Q_{i,\text{coll},c}$) the collection of rain (cloud droplets), $Q_{i,\text{shd}}$ the shedding, $Q_{i,\text{frz}}$ the refreezing, and $Q_{i,\text{dep}}$ is the vapor transfer. The latter can be a source term (condensation) or a sink term (evaporation). The source–sink terms are described in appendix A. Note, the modified definitions of $q_{i,\text{tot}}$ and $F_{i,\text{rim}}$ in (5) and (6), respectively, are consistent with P3_ORIG since, for $F_{i,\text{liq}} = 0$, these variables simply revert back to the original formulations in MM15.

b. Main assumptions

A major question when predicting $F_{i,\text{liq}}$ in bulk schemes is how the particle size evolves during melting. In traditional multimoment bulk parameterizations, the mean size of ice particles typically does not change during melting (e.g., Morrison et al. 2009; Thompson et al. 2008; Milbrandt and Yau 2005). This is a common closure assumption in order to calculate the decrease in number concentration during melting. However, observations show a decrease of size during melting for individual particles (Fujiyoshi 1986). This decrease can be captured by predicting $F_{i,\text{liq}}$. Past studies approximated the spherical drop equivalent diameter D_{eq} as a function of $F_{i,\text{liq}}$ and utilized a “melting critical diameter” D^* , such as Thériault and Stewart (2010) and Szyrmer and Zawadzki (1999). The melting critical diameter determines the largest particles in the

PSD that will melt completely within one time step, and it depends on $F_{i,\text{liq}}$. Thus, this method requires iteration to solve D_{eq} because of the interdependence of D^* and $F_{i,\text{liq}}$. This is one reason why this approach for the implementation of $F_{i,\text{liq}}$ has not been widely used in traditional bulk schemes designed with several solid precipitation categories.

Past theoretical and experimental studies have described the melting behavior of ice particles depending on their size and type. Rasmussen et al. (1984a) and Rasmussen and Pruppacher (1982) found that small spherical ice particles with $D < \sim 0.1$ cm melt quickly, in less than 1 min, into liquid drops. Fujiyoshi (1986) showed that the liquid water produced by the melting of unrimed nonspherical ice particles accumulates to form wet snow. Rasmussen et al. (1984b) found that a portion of the liquid produced by the melting of large rimed ice particles ($D > 0.1$ cm) is shed, while the rest is accumulated around the ice core. Leinonen and von Lerber (2018) showed that the melting of lightly rimed crystals is similar to the melting of unrimed aggregates (no shedding), whereas the melting of moderately rimed crystals is similar to the melting of graupel/hail (with shedding).

Based on Rasmussen et al. (1984a), all liquid water produced by the melting of small spherical ice particles ($D \leq D_{\text{th}}$) in P3_MOD is transferred to the rain category in one time step. Thus, it is assumed that D_{th} corresponds to the melting critical diameter in P3_MOD. For the parameter values of α_{va} and β_{va} used here, D_{th} is $\sim 66 \mu\text{m}$. Based on the studies discussed above, shedding during melting is considered when $F_{i,\text{rim}} > 0$, detailed in appendix A.

The simplest approach to describe the melting process is to assume that the liquid water is uniformly distributed around an ice core. For simplicity and because of a lack of detailed observations, ice cores are assumed to have the same properties (mass, projected area, capacitance, ventilation coefficient, and so on) as in P3_ORIG. Melting decreases ice-core mass $q_{i,\text{ice}}$ but not the total ice number $N_{i,\text{tot}}$, except for particles with $D \leq D_{\text{th}}$ that are transferred to the rain category as described above; thus, the mean size of ice cores decreases during melting. Because the bulk ice particle density increases with decreasing particle size in P3, this assumption is physically reasonable and implies a tendency toward small spherical ice cores with a density equal to ρ_i as particles melt.

According to the assumptions below, the most straightforward approach for the implementation of $F_{i,\text{liq}}$ into P3 is to separate processes based on whether they apply to the ice core embedded within the particle or the whole mixed-phase particle (liquid and ice). This way, each process can be integrated over the appropriate size distribution based on the microphysical process computed. It is assumed that

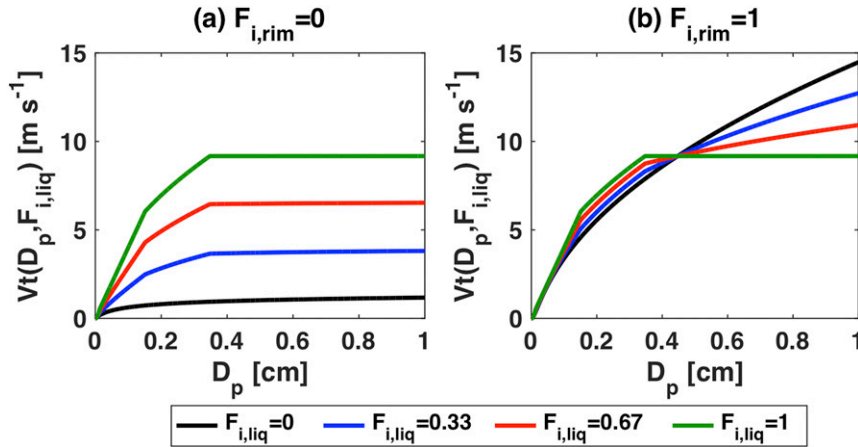


FIG. 1. Terminal velocity of P3_MOD [$V_t(D_p, F_{i,liq}); \text{m s}^{-1}$] as a function of the full particle diameter D_p (cm) when the bulk rime mass fraction $F_{i,rim}$ is (a) 0 and (b) 1, and the bulk liquid mass fraction $F_{i,liq}$ is 0 (black), 0.33 (blue), 0.67 (red), and 1 (green).

melting depends directly on properties of the ice core embedded in mixed-phase particles. Thus, the bulk melting rate (detailed in appendix A) is calculated by integration over the PSD computed using the ice-core diameter D_d . Ice-core PSD parameters $N_{0,core}$, μ_{core} , and λ_{core} are computed using $q_{i,ice} = (1 - F_{i,liq})q_{i,tot}$ and $m_d(D)$ following (3a)–(3d). Note that sublimation/deposition processes also depend directly on properties of the ice core embedded in the whole particle, as explained in appendix A.

Other microphysical processes, such as refreezing, condensation/evaporation of the liquid component, self-collection, shedding, and collection with other particle categories depend on properties of the whole particle (both the ice and liquid components). Bulk rates for these processes (also detailed in appendix A) are calculated by integrating over the PSD computed using the full mixed-phase particle diameter D_p . To compute the whole particle PSD parameters $N_{0,p}$, μ_p , and λ_p , the mass–diameter relationship $m_t(D_p, F_{i,liq})$ is needed. For simplicity and because of lack of observations, it is assumed that at a given D_p , $m_t(D_p, F_{i,liq})$ is calculated by a linear interpolation based on $F_{i,liq}$:

$$m_t(D_p, F_{i,liq}) = (1 - F_{i,liq})m_d(D_p) + F_{i,liq}m_{liq}(D_p). \quad (10)$$

Here, $m_d(D_p)$ is given by (3a) to (3d) and $m_{liq}(D_p) = (\pi/6)\rho_w D_p^3$ ($\rho_w = 1000 \text{ kg m}^{-3}$), evaluated over the full mixed-phase PSD (from 0 to ∞). The relationship $m_t(D_p, F_{i,liq})$ is used to solve the PSD parameters $N_{0,p}$, μ_p , and λ_p over $q_{i,tot}$ defined by

$$q_{i,tot} = \int_0^\infty m_t(D_p, F_{i,liq}) N_{0,p} D_p^{\mu_p} \exp(-\lambda_p D_p) dD_p. \quad (11)$$

The linear interpolation of $F_{i,liq}$ for $m_t(D_p, F_{i,liq})$ is consistent with a density of the mixed-phase particle being equal to a $F_{i,liq}$ -weighted average of the ice and liquid parts, which was also used by Szyrmer and Zawadzki (1999). Also, this approach is consistent with 1) assuming a constant $F_{i,liq}$ with diameter over the size distribution, 2) physically consistent behaviors in the limits of $F_{i,liq} = 0$ and $F_{i,liq} = 1$, 3) a mixed-phase particle density that must always be less than or equal to the density of a liquid drop with the same diameter, and 4) a straightforward computation of the size distribution parameters as a function of $F_{i,liq}$.

An approach similar to (10) is made for the projected area $A_t(D_p, F_{i,liq})$ and for the terminal velocity $V_t(D_p, F_{i,liq})$ relationships. These are, respectively,

$$A_t(D_p, F_{i,liq}) = (1 - F_{i,liq})A_d(D_p) + F_{i,liq}A_{liq}(D_p), \quad (12)$$

where $A_d(D_p)$ is the P3_ORIG projected-area relationships, $A_{liq}(D_p) = (\pi/4)D_p^2$, and

$$V_t(D_p, F_{i,liq}) = (1 - F_{i,liq})V_t(D_p, F_{i,liq} = 0) + F_{i,liq}V_t(D_p, F_{i,liq} = 1), \quad (13)$$

where $V_t(D_p, F_{i,liq} = 0)$ and $V_t(D_p, F_{i,liq} = 1)$ are given in appendix B [(B4) and (B6), respectively, but with D_d replaced by D_p]. These expressions follow Mitchell and Heymsfield (2005) and Simmel et al. (2002), respectively.

The $V_t(D_p, F_{i,liq})$ of unrimmed ice ($F_{i,rim} = 0$) and fully rimmed ice ($F_{i,rim} = 1$) at four different values of $F_{i,liq}$ are shown in Figs. 1a and 1b, respectively. The terminal velocity increases with both the particle size D_p and $F_{i,liq}$ in agreement with the observations of M90 for unrimmed

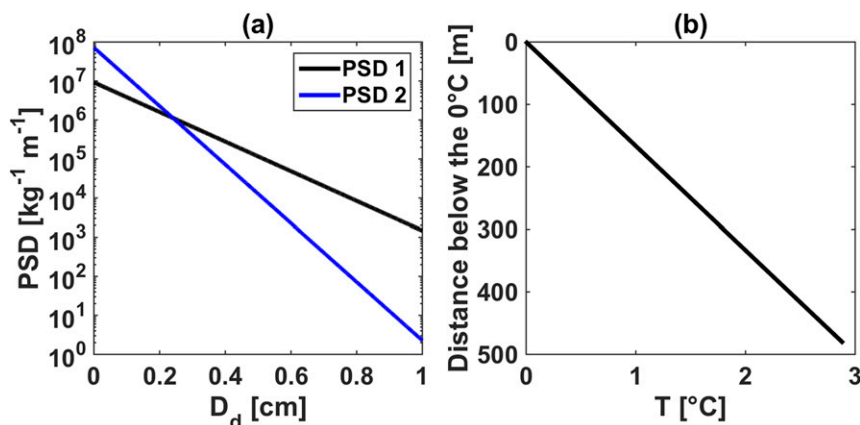


FIG. 2. Initial conditions used for the melting-rate tests comparing P3_MOD and the Lagrangian M90 model: (a) the initial PSD 1 (black; $\text{kg}^{-1} \text{m}^{-1}$) and PSD 2 (blue; $\text{kg}^{-1} \text{m}^{-1}$); (b) the vertical temperature T ($^{\circ}\text{C}$) profile below the 0°C .

ice (Fig. 1a). Direct comparison with the observed and experimental terminal velocities of M90 is, however, difficult because the M90 relationship can only be applied to unrimed ice particles. Also, the M90 fall speed relationship used a different ice-core mass–dimension relationship compared to P3. There are no observations of terminal velocities of partially melted rimed (partially or fully) ice particles. Based on Rasmussen et al. (1984b), it is assumed that for large particles, accumulated liquid water is shed. However, for unrimed and partially rimed ice, the liquid water is retained and forms a shell, which flattens as the particles fall, thereby limiting the increase of fall speed with D_p similar to the behavior of large purely liquid drops. This is seen in Fig. 1b for particles larger than 0.4 cm.

4. Comparison with a benchmark melting model

a. Experimental design

A benchmark comparison of P3_MOD with a detailed Lagrangian model using the M90 microphysics parameterization is presented. It aims at illustrating differences between P3_MOD and M90 in the melting behavior of a population of ice particles. M90, Yokoyama and Tanaka (1984), and Matsuo and Sayso (1981) have evaluated the distance below the 0°C level for a single falling ice crystal to melt completely using a Lagrangian model with their respective melting equations. Here, this distance is evaluated for a population of unrimed nonspherical ice particles to calculate the evolution of melting particles as they fall, with comparison between the P3_MOD scheme and a Lagrangian model we developed with the M90 parameterization. Two different populations of ice particles, shown in Fig. 2a, provide

input boundary conditions. The first, PSD 1, includes a moderate number of large ice particles characterized by a total ice mass mixing ratio of $q_{i,\text{tot}} = 0.6 \text{ g kg}^{-1}$ and a total number mixing ratio of ice of $N_{i,\text{tot}} = 10\,550 \text{ kg}^{-1}$. The second, PSD 2, includes a larger number of small ice particles characterized by $q_{i,\text{tot}} = 0.65 \text{ g kg}^{-1}$ and $N_{i,\text{tot}} = 41\,550 \text{ kg}^{-1}$. Rimed particles are not included in this experiment because they are not accounted for in the M90 parameterization.

Both the Lagrangian benchmark and P3_MOD bulk model use the melting equation developed in appendix A [see (A3)]. To solve (A3), both models use a temperature variation with height of $0.6^{\circ}\text{C} (100 \text{ m})^{-1}$ as shown in Fig. 2b. For both models, melting is the only microphysical process included, and feedback between temperature and latent cooling during melting is neglected; the temperature profile is constant in time. The parameters L_e , L_f , k_a , D_v , $q_{s,0}$, q_v , and ρ_a are computed with the air temperature and pressure, assuming hydrostatic balance. The atmosphere is saturated with respect to water.

The Lagrangian model solves (A3) using the M90 parameterization. It is numerically integrated as an initial-value problem using a simple Euler forward scheme with a time step of 1 s. The model is initialized by dividing the particle population into 10 000 particle sizes with varying D_d , covering a size range from 0.0001 to 2 cm. This provides the evolution of particle properties along vertical trajectories for each of the 10 000 initial sizes. Bulk properties of the model, such as $F_{i,\text{liq}}$ and $q_{i,\text{ice}}$, are calculated from these trajectories every meter below the 0°C level. The particle fall speed follows from M90 [Geresdi et al. 2014; see their (3)].

P3_MOD solves bulk equations for the 1D (vertical) model prognostic variables as they evolve in time.

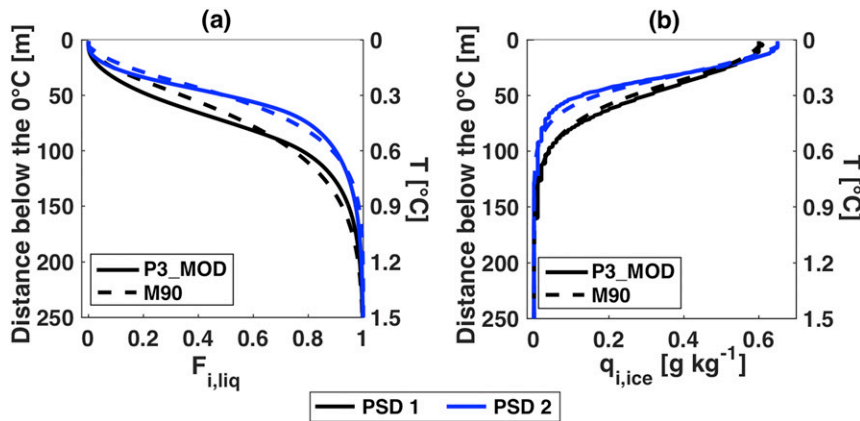


FIG. 3. P3_MOD (solid) and the Lagrangian M90 model (dashed) variations below the 0°C isotherm of (a) the bulk liquid mass fraction $F_{i,liq}$ and (b) the ice mass mixing ratio $q_{i,ice}$ (g kg^{-1}) for the initial PSD 1 (black) and the initial PSD 2 (blue).

Sedimentation is calculated using a simple first-order upwind approach using the mean number- and mass-weighted bulk fall speeds described in appendix A. The equations are solved using a time step of 1 s and a vertical grid spacing of 1 m. Results for comparison with the Lagrangian model are taken after 10 min of simulation time.

b. Results

Plots of $F_{i,liq}$ and the $q_{i,ice}$ as a function of the distance below the 0°C level are shown in Figs. 3a and 3b, respectively. Overall, the Lagrangian benchmark model and P3_MOD give similar results. For a given T , differences in $F_{i,liq}$ between P3_MOD and the Lagrangian model are always smaller than 0.15 and relatively larger for small $F_{i,liq}$. The melting process in P3_MOD is somewhat slower than the Lagrangian model for $F_{i,liq} < 0.6-0.7$, leading to a slightly larger $q_{i,ice}$ in P3_MOD. This is compensated by slightly faster melting in P3_MOD for larger $F_{i,liq}$ so that the total distance for melting is nearly the same as in the Lagrangian model.

The small differences between P3_MOD and the Lagrangian model seen in Fig. 3 can be explained mainly by differences in the parameterization used for the melting equation associated with the capacitance $C(D_d, F_{i,liq})$ and ventilation coefficient $F(D_d, F_{i,liq})$ relationships. For the Lagrangian model, the M90 relationships are based on Pruppacher and Klett (1997). For P3_MOD, the relationships are given in appendix B [(B1) and (B2), respectively]. Figure 4 shows comparisons between M90 and P3_MOD of the capacitance (Fig. 4a) and the ventilation coefficient (Fig. 4b) for unrimed ice ($F_{i,rim} = 0$). At a given D_d , the capacitance of P3_MOD is slightly smaller than M90, especially at low $F_{i,liq}$. Larger differences occur for the ventilation coefficient owing to its dependence on the

terminal velocity parameterization in (A3). For a given D_d , the ventilation coefficient of P3_MOD is greater (smaller) than M90 at low (high) $F_{i,liq}$. As detailed in appendix B, the ventilation coefficient for P3_MOD is computed by linear interpolation as a function of $F_{i,liq}$ between the ventilation parameters for dry ice in P3_ORIG when $F_{i,liq} = 0$ and those corresponding to a liquid drop when $F_{i,liq} = 1$. On the other hand, in M90, the ventilation coefficient is computed using their experimental terminal velocity, which is small at low $F_{i,liq}$ and increases quickly at $F_{i,liq} > 0.7$. Also seen in Fig. 3, the differences between P3_MOD and the Lagrangian model using M90 are larger for PSD 1 than for PSD 2, especially when $F_{i,liq}$ is small. This is because PSD 1 has a higher concentration of large particles, and differences in the ventilation coefficient parameterization between P3_MOD and M90 are greater for larger particles than smaller ones (Fig. 4b).

A comparison between M90 Lagrangian model and P3_MOD for the evolution of the PSDs as the two populations of ice particles fall below the 0°C is shown in Fig. 5. Note that the PSDs in Fig. 5 are shown as a function of the ice-core diameter D_d . For both initial PSDs 1 and 2 from P3_MOD, the shape parameter of the gamma PSD remains unchanged and is equal to 0 at small liquid fractions. However, when the liquid fraction increases, the slope parameter increases, which leads to an increase of the shape parameter. This behavior is seen with PSD 2 at $F_{i,liq} = 0.9$. The intercept parameter also increases with $F_{i,liq}$ for both PSDs. In general, the three parameters of the PSD increase with the increasing $F_{i,liq}$, and their changes depend on the rime mass fraction and the values of $q_{i,tot}$ and $N_{i,tot}$ that characterize the PSD. The evolution of the PSDs for the P3_MOD simulations compares well to that using

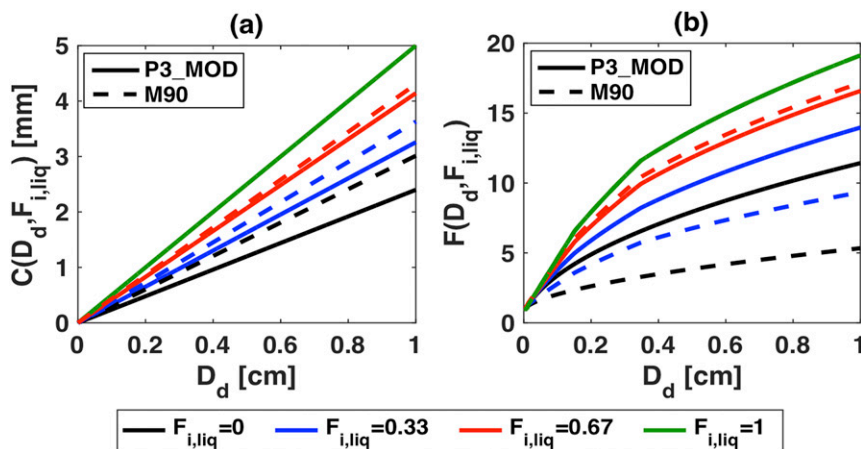


FIG. 4. P3_MOD (solid) and the Lagrangian M90 model (dashed) (a) capacitance $C(D_d, F_{i,liq})$ (mm) and (b) ventilation coefficient $F(D_d, F_{i,liq})$ as a function of the maximum dimension of the ice core D_d (cm) when the bulk rime fraction is 0 and the bulk liquid mass fraction $F_{i,liq}$ is 0 (black), 0.33 (blue), 0.67 (red), and 1 (green).

the M90 Lagrangian model, especially at low $F_{i,liq}$, and reflects the decrease of particle size and shift of the PSD toward smaller sizes during melting (Thériault and Stewart 2010; Thériault et al. 2006). Overall, these simulations suggest that P3_MOD behaves realistically compared to M90.

Instead of comparing with the Lagrangian M90 model, the P3_MOD melting process for $F_{i,rime} = 0$ could also be compared to the Thériault and Stewart (2010) bulk microphysics scheme. It is believed that results will be comparable, since Thériault and Stewart (2010) used the same parameterizations as M90. However, as the parameterizations are very different between

Thériault and Stewart (2010) and P3_MOD, and the Thériault and Stewart (2010) scheme does not include the prediction of rime fraction, P3_MOD will only be compared to P3_ORIG in the following.

5. Idealized simulations using P3_MOD

a. Experimental design

Characteristics of the precipitation type are investigated using P3_MOD coupled with a simple 1D kinematic model. P3_MOD is compared to P3_ORIG to illustrate differences in the precipitation properties

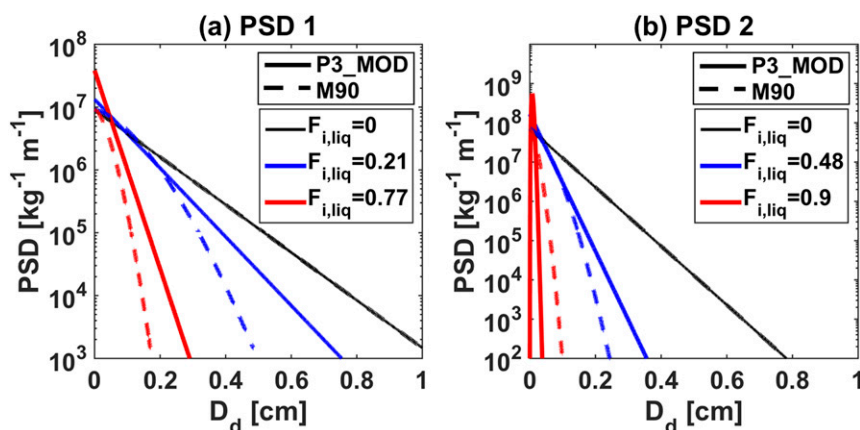


FIG. 5. P3_MOD (solid) and the Lagrangian M90 model (dashed) vertical evolution of the PSD ($\text{kg}^{-1} \text{m}^{-1}$) below the 0°C isotherm for (a) initial PSD 1 at bulk liquid mass fractions $F_{i,liq} = 0$ (black), 0.21 (blue), and 0.77 (red) and (b) initial PSD 2 at bulk liquid mass fractions $F_{i,liq} = 0$ (black), 0.48 (blue), and 0.9 (red). The three liquid mass fractions correspond to heights (temperatures) of 0 m (0°C), 50 m (0.3°C), and 100 m (0.6°C), respectively, in P3_MOD.

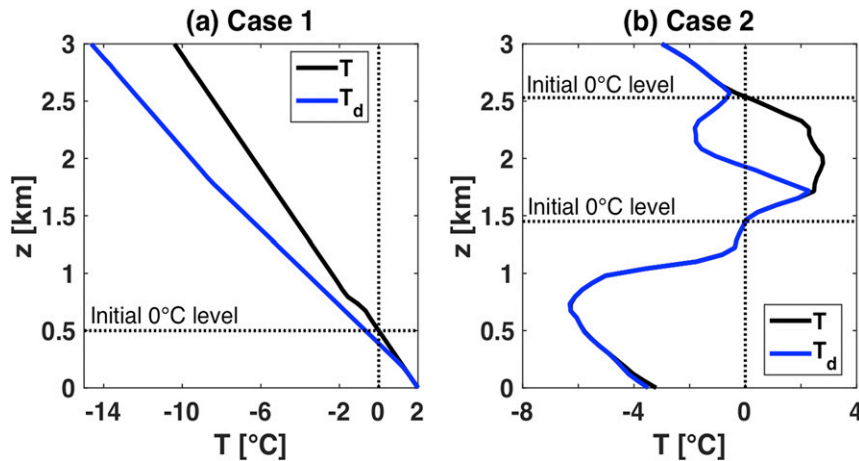


FIG. 6. Initial vertical profiles of temperature T (black; °C) and dewpoint temperature T_d (blue; °C) for (a) case 1 and (b) case 2. Horizontal dotted lines show the initial 0°C level.

with the prediction of the $F_{i,liq}$ and the overall behavior of the modified scheme.

All 1D simulations are initialized with vertical profiles of temperature and water vapor mass mixing ratio for 50 vertical levels evenly spaced. The grid spacing is 60 m. The simulated period is 2 h, and the time step is 1 s. Hydrostatic balance is assumed. The precipitation type characteristics are analyzed after 90 min of simulation time. A total ice mass mixing ratio of $q_{i,tot} = 0.265 \text{ g kg}^{-1}$ and total ice number mixing ratio of $N_{i,tot} = 5000 \text{ kg}^{-1}$ provide boundary conditions at the domain top. This corresponds to a snowfall rate of 1 mm h^{-1} when $F_{i,rim} = 0$. Sensitivity of the precipitation properties to variation of the $F_{i,rim}$ value specified at the domain top is also investigated. The initial $q_{i,rim}$, with a fixed bulk rime density of 900 kg m^{-3} , is systematically modified to increase the snowfall rate at the top of the column such that it reaches 2.7 mm h^{-1} when $F_{i,rim} = 1$; the increased snowfall rate for a given $q_{i,tot}$ occurs because the mass-weighted mean fall speed increases with $F_{i,rim}$. The vertical air motion is zero throughout the column.

Two observed vertical profiles of temperature and dewpoint temperature were used to initialize the 1D simulations, shown in Fig. 6. Case 1 (Fig. 6a) has a vertical profile that was measured by a gondola during the Science of Nowcasting Olympic Weather for Vancouver 2010 (SNOW-V10; Isaac et al. 2014) field campaign. It is characterized by melting near the surface. A rain–snow boundary was observed along Whistler Mountain at around 2300 UTC 7 March 2010 (Thériault et al. 2014), with a mixture of wet snow and rain at the base of the mountain. In this profile, the near-surface melting layer is 500 m deep, and the environmental conditions are subsaturated with respect to liquid water in cold layers and at the melting-layer top.

The case 2 (Fig. 6b) thermodynamic profile is based on observations obtained on 2315 UTC 1 February 1992 at St. John’s, Newfoundland, Canada (Hanesiak and Stewart 1995). It is associated with a melting layer atop a refreezing layer below. A mixture of ice pellets and some needles were reported at the surface around 2317 UTC, and a mixture of ice pellets, freezing rain, and needles at around 2345 UTC. In the refreezing layer of this profile, the environmental conditions are near saturation with respect to liquid water, meaning that it is supersaturated with respect to ice. The top of the melting layer is subsaturated with respect to liquid water.

b. Case 1: Melting layer near the surface

Vertical profiles of the temperature, mass and number mixing ratios, liquid fraction, and mass-weighted density and fall speed after 90 min are shown in Fig. 7 for both P3_ORIG and P3_MOD. These results are for unrimed ice; that is, $F_{i,rim} = 0$ at the domain top. The main microphysical processes (not shown) for both simulations are sublimation in the cold layers ($T < 0^\circ\text{C}$) and melting in the warm layers. Collection of rain and evaporation occur in the warm layer, with evaporation of melting ice neglected in P3_ORIG. In P3_MOD, these processes are sources and sinks for the liquid component, $q_{i,liq}$. Collected rain in P3_ORIG is shed back to rain at temperatures above freezing, while in P3_MOD, the collected rain is added to $q_{i,liq}$. The evaporation of $q_{i,liq}$ in P3_MOD cools the air near the top of the melting layer compared to P3_ORIG (Fig. 7a). The surface precipitation type formed in P3_ORIG is rain (Fig. 7b), while in P3_MOD, there is a mixture of rain and almost completely melting ice (Fig. 7b), the latter characterized by $F_{i,liq} = 0.98$ (Fig. 7d). The total number mixing ratio of rain (Fig. 7c) is higher in P3_MOD compared to P3_ORIG because the source

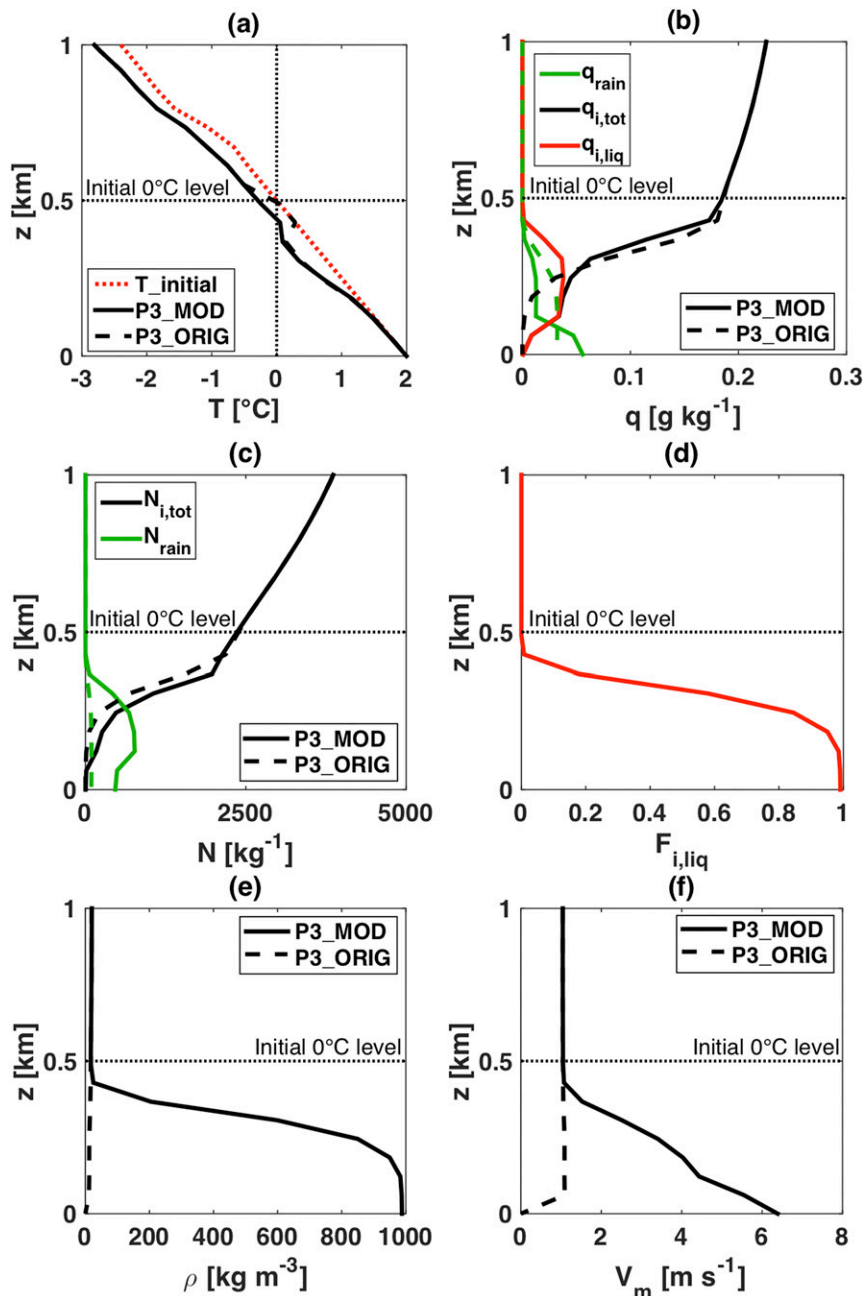


FIG. 7. P3_MOD (solid) and P3_ORIG (dashed) vertical profiles of (a) temperature T ($^{\circ}\text{C}$); (b) mixing ratios q (g kg^{-1}) of rain mass (green), total ice/mixed-phase particle mass (black), and accumulated liquid mass on ice (red); (c) total number mixing ratios N (kg^{-1}) of ice (black) and rain (green); (d) bulk liquid mass fraction of P3_MOD $F_{i,\text{liq}}$; (e) mean mass-weighted density ρ (kg m^{-3}); and (f) mean mass-weighted fall speed V_m (m s^{-1}) produced at $t = 90$ min. The red dotted line in (a) shows the initial profile of temperature (T_{initial} ; $^{\circ}\text{C}$). The horizontal dotted lines show the height of the initial 0°C isotherm. The rime mass fraction at the model top is $F_{i,\text{rim}} = 0$ for both P3_MOD and P3_ORIG.

term for rain number concentration is parameterized differently. In P3_ORIG, the rain number source from melting is proportional to the respective changes in $q_{i,\text{tot}}$, while it is proportional to $q_{i,\text{ice}}$ in P3_MOD (appendix A).

Moreover, P3_ORIG calculates the number of raindrops formed by melting using a scaling factor of 0.2 to account for the rapid evaporation of small melting particles; that is, it assumes a proportion of one raindrop formed per five

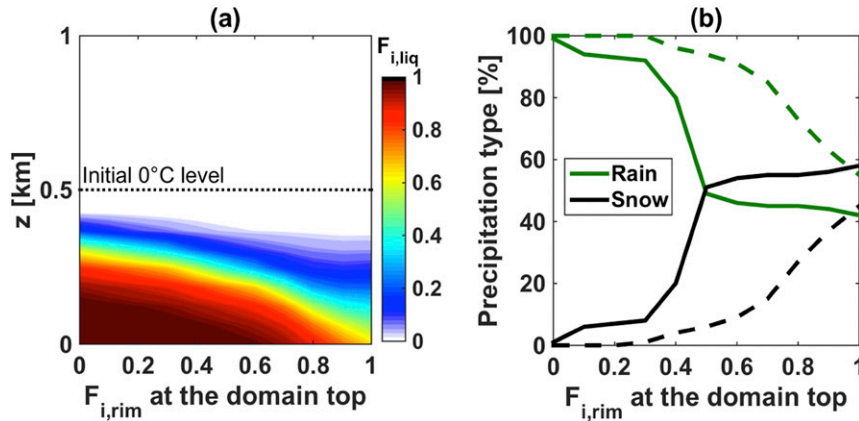


FIG. 8. (a) Vertical variation of the bulk liquid mass fraction $F_{i,liq}$ (colors) as a function of the rime mass fraction $F_{i,rim}$ at the domain top at $t = 90$ min. (b) P3_MOD (solid) and P3_ORIG (dashed) surface precipitation type relative to the total surface precipitation (%) for ice (black) and rain (green) produced at $t = 90$ min as a function of the specified $F_{i,rim}$ at the domain top.

melted ice particles. No such scaling is applied in P3_MOD. Both mass-weighted density (Fig. 7e) and fall speed (Fig. 7f) are larger in P3_MOD compared to P3_ORIG in the melting layer, which has significant impacts on the melting time of particles; faster fall speeds mean less time to melt over a given distance.

Results from varying the rime mass fraction $F_{i,rim}$ specified at the domain top are shown in Figs. 8 and 9. Vertical profiles of $F_{i,liq}$ after 90 min (Fig. 8a) illustrate that at low $F_{i,rim}$, particles melt almost completely before reaching the surface. This is reflected by the percentages of surface precipitation types reaching the surface (Fig. 8b). The surface precipitation type is only rain using P3_ORIG for an initial $F_{i,rim} \leq 0.2$, while P3_MOD produces a mixture of rain and very wet ice of $F_{i,liq} > 0.95$. For initial values of $F_{i,rim} > 0.5$, both P3_ORIG and P3_MOD show a mixture of surface precipitation types. Differences between P3_ORIG and P3_MOD are mainly due to collection of rain, shedding, and the production of faster-falling particles by P3_MOD. For example, the collection of rain by partially melted ice increases with the specified $F_{i,rim}$ at the domain top because there is more shedding, which reduces the amount of rain reaching the surface in P3_MOD. Also, as seen in Fig. 9, an increase of the mean mass-weighted density (Fig. 9a) and the mean mass-weighted fall speeds (Fig. 9c) occurs in P3_MOD compared to P3_ORIG (Figs. 9b and 9d, respectively), which, as mentioned before, impacts the time spent by particles in the warm layer. The main added value of P3_MOD for this case is the ability to produce wet snow at the surface.

c. Case 2: Melting layer aloft

Results for case 2, specifying $F_{i,rim} = 1$ at the domain top, are shown in Fig. 10. As for case 1, only melting

cools the environmental air in P3_ORIG, while there is also cooling from evaporation of $q_{i,liq}$ in P3_MOD at the top of the melting layer (Fig. 10a). In both P3_ORIG and P3_MOD, a mixture of supercooled raindrops and rimed ice is produced in the refreezing layer (Fig. 10b). Note that supercooled raindrops represent freezing rain as the surface temperature is $< 0^\circ\text{C}$ in both P3_MOD and P3_ORIG. Note also that since $F_{i,rim} = 1$, the lines for $q_{i,tot}$ and $q_{i,rim}$ are superimposed for P3_ORIG. In P3_MOD, rimed ice is produced from the complete refreezing of partially melted ice aloft, which is the process forming ice pellets. The proportion of ice to the total precipitation is higher in P3_MOD compared to P3_ORIG because of the partial melting and the refreezing of partially melted ice, which is neglected in P3_ORIG. Values of $F_{i,liq}$ for partially melted ice entering the cold layer are ~ 0.8 and decrease below 1.2 km because of refreezing (Fig. 10d). The rime mass fraction (Fig. 10d) remains close to 1 and the rime density (Fig. 10e) to 900 kg m^{-3} at all heights, which follows from the parameterization of melting and refreezing as described in appendix A. The mass-weighted mean density (Fig. 10e) and fall speed (Fig. 10f) increase in the warm layer and slightly decrease in the cold layer, the latter associated with ice pellets.

The temporal evolutions of P3_MOD and P3_ORIG air temperature are shown in Figs. 11a and 11b, respectively. Cooling due to melting and warming due to refreezing are the main processes affecting temperature, giving profiles that tend toward a 0°C isothermal layer. P3_MOD is generally colder in the melting layer and warmer in the refreezing layer than P3_ORIG (Fig. 11c). The formation of ice pellets by refreezing in P3_MOD

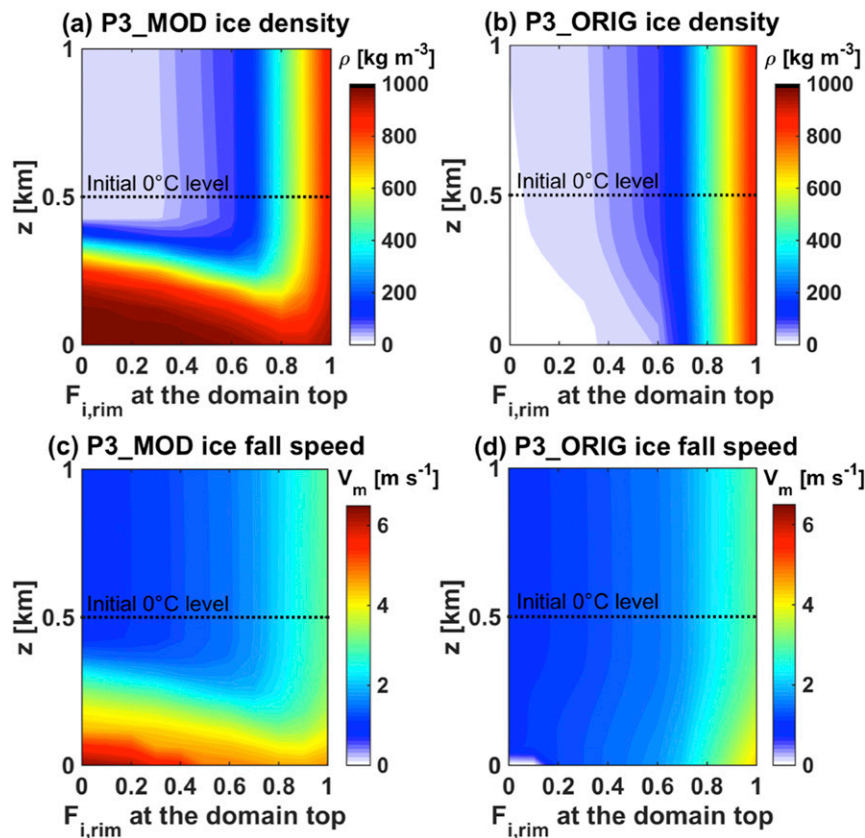


FIG. 9. (a),(c) P3_MOD and (b),(d) P3_ORIG vertical variations of (a),(b) the mean mass-weighted bulk density ρ (kg m^{-3}) and (c),(d) the mean mass-weighted fall speed V_m (m s^{-1}) at $t = 90$ min as function of the rime mass fraction $F_{i,\text{rim}}$ at the domain top.

warms the air compared to P3_ORIG. Differences in the melting layer are associated with faster-falling particles when $F_{i,\text{liq}} > 0$ after the onset of melting in P3_MOD, which vertically extends the region where particles melt compared to P3_ORIG. In the cold layer, temperature differences are larger because of refreezing in P3_MOD, which does not occur in the P3_ORIG simulation.

Percentages of surface precipitation types from varying $F_{i,\text{rim}}$ at the domain top for case 2 are shown in Fig. 12. For $F_{i,\text{rim}} \leq 0.6$ at the domain top, both P3_MOD and P3_ORIG produce only freezing rain at the surface over the entire period. For $F_{i,\text{rim}} \geq 0.6$ at the model top, both P3_MOD and P3_ORIG show a mixture of ice and freezing rain. However, ice pellets formed from refreezing are the dominant precipitation type in P3_MOD when $F_{i,\text{rim}} > 0.65$ at the model top, whereas freezing rain is the dominant type in P3_ORIG. The refreezing process in P3_MOD has a major impact on the precipitation types reaching the surface because the generation of ice pellets from refreezing leads to an increase in the

collection of supercooled raindrops, in turn reducing freezing rain at the surface consistent with Barszcz et al. (2018).

6. Summary and conclusions

A new parameterization approach is proposed to predict the bulk liquid mass fraction of mixed-phase particles, $F_{i,\text{liq}}$, in the predicted particle properties (P3) bulk microphysics scheme. The modified scheme, P3_MOD, can explicitly simulate the evolution of bulk mixed-phase particle properties, thus improving the representation of key microphysical processes such as melting, evaporation/condensation, and refreezing. It also allows the explicit prediction of several winter precipitation types, such as freezing rain, ice pellets, and wet snow because of the addition of a new prognostic variable, the bulk liquid mass mixing ratio accumulated on ice $q_{i,\text{liq}}$.

P3_MOD produced comparable melting rates to a Lagrangian benchmark model based on the M90 melting parameterization, which was developed from

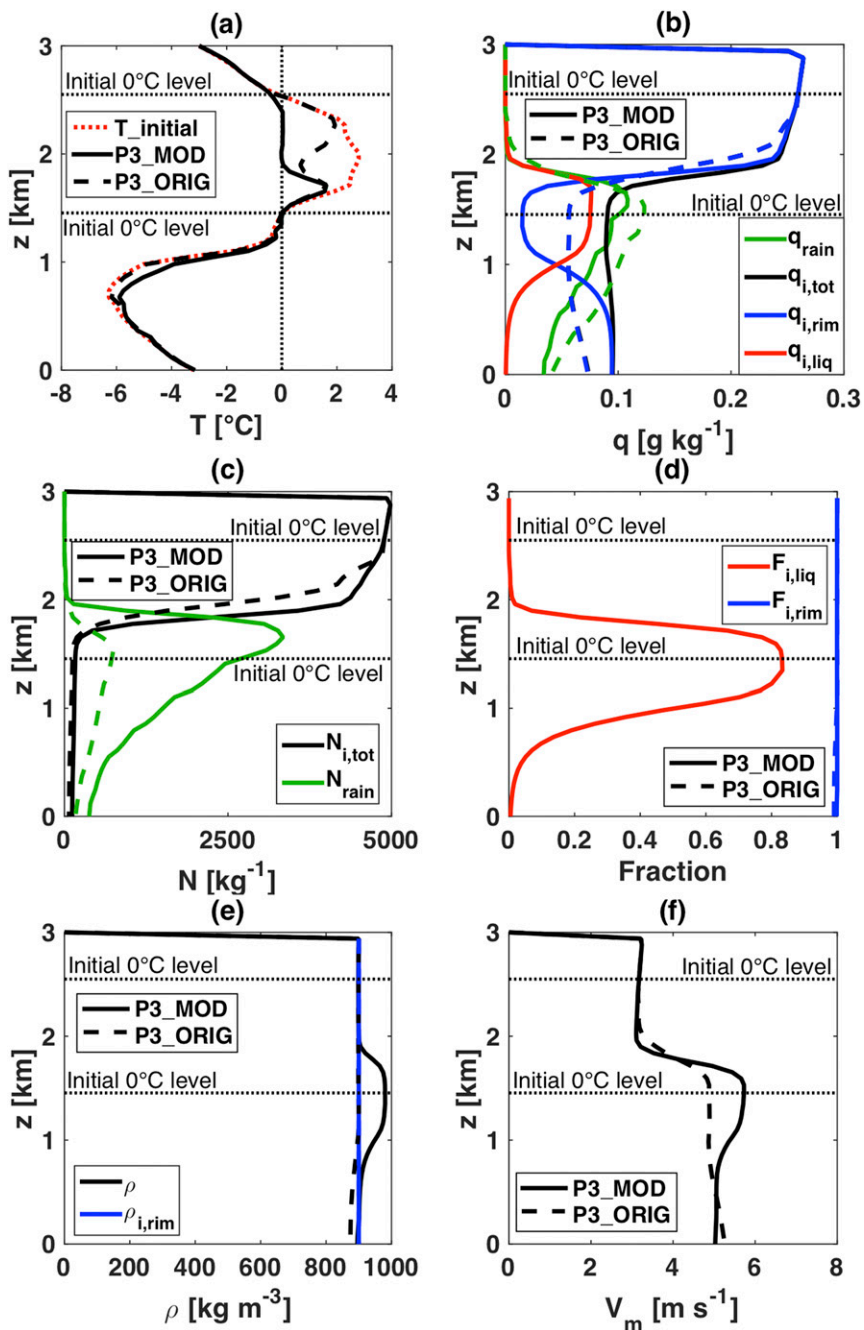


FIG. 10. P3_MOD (solid) and P3_ORIG (dashed) vertical profiles of (a) temperature T ($^{\circ}\text{C}$); (b) mixing ratios q (g kg^{-1}) of rain mass (green), total ice/mixed-phase particle mass (black), rime ice mass (blue), and accumulated liquid mass on ice (red); (c) total number mixing ratios N (kg^{-1}) of ice (black) and rain (green); (d) bulk liquid $F_{i,\text{liq}}$ (red) and rime $F_{i,\text{rim}}$ (blue) mass fractions; (e) mean mass-weighted density ρ (black; kg m^{-3}) and bulk rime density $\rho_{i,\text{rim}}$ (blue; kg m^{-3}); and (f) mean mass-weighted fall speed V_m (m s^{-1}) produced at $t = 90$ min. The red dotted line in (a) shows the initial profile of temperature (T_{initial} ; $^{\circ}\text{C}$). The horizontal dotted lines show the height of the initial 0°C isotherm. The rime mass fraction at the domain top is 1 for both P3_MOD and P3_ORIG.

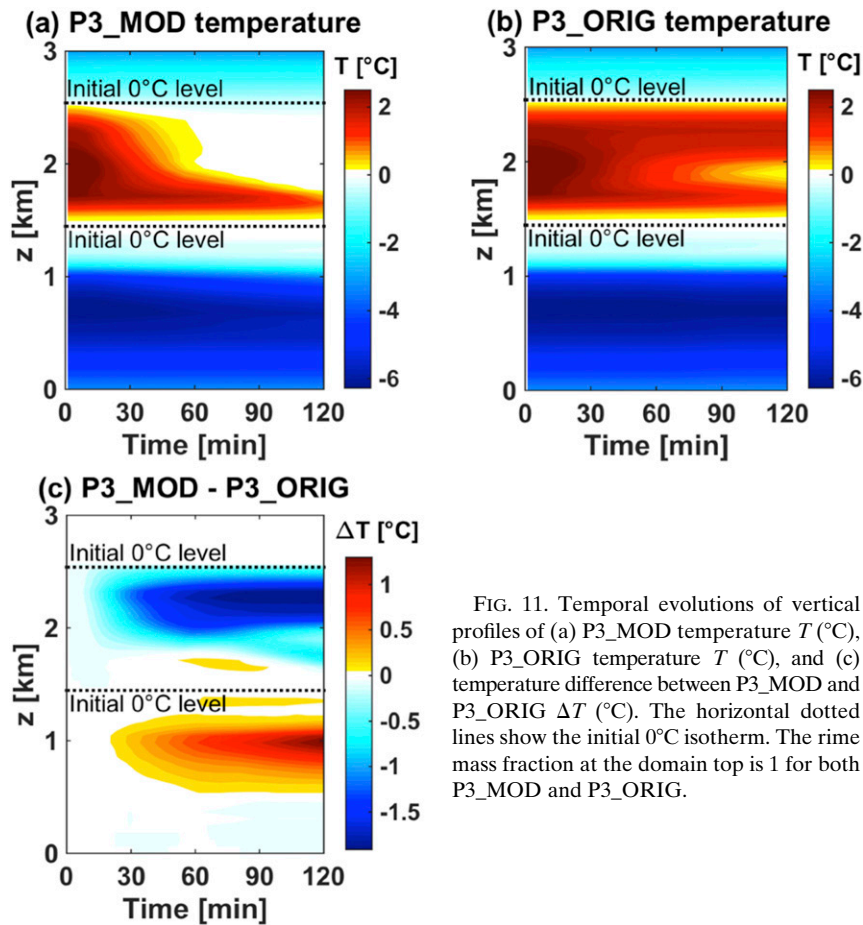


FIG. 11. Temporal evolutions of vertical profiles of (a) P3_MOD temperature T ($^{\circ}\text{C}$), (b) P3_ORIG temperature T ($^{\circ}\text{C}$), and (c) temperature difference between P3_MOD and P3_ORIG ΔT ($^{\circ}\text{C}$). The horizontal dotted lines show the initial 0°C isotherm. The rime mass fraction at the domain top is 1 for both P3_MOD and P3_ORIG.

observations. This supports the viability of P3_MOD and its bulk representation of the melting behavior of ice particles. Prediction of the liquid fraction affects the mean fall speed and density of hydrometeors falling into a melting layer, which in turn impacts distributions of latent cooling as well as other microphysical processes such as collection and condensation/evaporation, compared to P3_ORIG. Predicting the liquid fraction also allows the refreezing of partially melted ice particles to be explicitly represented, which increases the formation of ice pellets and the ratio of ice pellets to supercooled rain compared to P3_ORIG. Finally, the sensitivity of surface precipitation characteristics to riming differs between P3_MOD and P3_ORIG. For a melting layer 500 m deep and a surface temperature of 2°C , an increase in rime mass fraction leads to an increase in the ratio of snow to liquid precipitation in P3_MOD compared to P3_ORIG.

Overall, implementation of the bulk liquid fraction in P3 is a step forward toward better prediction of precipitation type and distribution when the temperature is near 0°C . Important precipitation types,

such as ice pellets and hail, involve tracking mixed-phase particles. Forecasting these precipitation types will therefore benefit from the prediction of the bulk liquid fraction. Although the focus of this work is on improving the representation of wintertime mixed-phase precipitation, the parameterized microphysics in P3_MOD is general and thus the inclusion of the predicted liquid fraction should also improve the simulation of hail through better representation of shedding during wet growth and melting. The effects of P3_MOD on the simulation of hail will be examined in a future study. Since P3_MOD only involves one additional prognostic variable per ice category, the additional computational cost is relatively small. It could be used in numerical weather prediction (NWP) as well as in convection-permitting climate models (CPCM).

Although the main objective of the paper was to describe the new approach for implementing $F_{i,\text{liq}}$ into P3, and we show that the approach is comparable to the detailed Lagrangian model, comparison with observations is needed to validate the new parameterization. Therefore, in future work, P3_MOD will be tested by

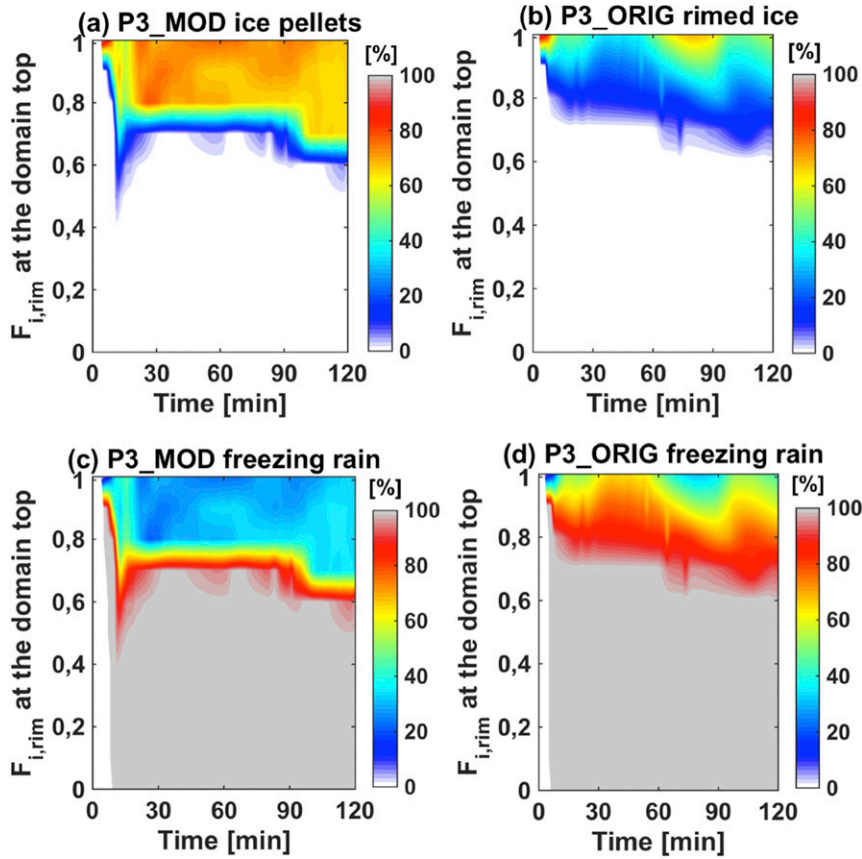


FIG. 12. Temporal evolution of the surface precipitation type relative to the total surface precipitation (%) of (a) P3_MOD ice pellets, (b) P3_ORIG rimed ice, (c) P3_MOD freezing rain, and (d) P3_ORIG freezing rain as a function of the initial rime mass fraction $F_{i,rim}$.

simulating a freezing rain and ice pellets storm using a three-dimensional atmospheric model, with comparison to detailed observations.

Acknowledgments. The authors would like to thank the Canadian Network for Regional Climate and Weather Processes (CNRCWP) and the NSERC Discovery grant for funding this research. One of the authors (Mélissa Cholette) would like to thank the Fonds de Recherche du Québec—Nature et Technologies (FQRNT) and the UQAM Faculty of Science for graduate fellowships. We would like to thank the three anonymous reviewers for their constructive comments.

APPENDIX A

The Microphysical Process Formulations

a. Melting

The melting source/sink is divided into two terms. The first term is the meltwater transferred to the rain

category $Q_{r,mlt}$, and the second is the meltwater accumulated on ice particles $Q_{i,mlt}$:

$$Q_{r,mlt} = \int_0^{D_{th}} \left. \frac{dm_{ice}}{dt} \right|_{melting} N_{0,core} D_d^{\mu_{core}} \exp(-\lambda_{core} D_d) dD_d, \quad (A1)$$

$$Q_{i,mlt} = \int_{D_{th}}^{\infty} \left. \frac{dm_{ice}}{dt} \right|_{melting} N_{0,core} D_d^{\mu_{core}} \exp(-\lambda_{core} D_d) dD_d, \quad (A2)$$

where D_d is the maximum dimension of the ice core and $(dm_{ice}/dt)|_{melting}$ is the melting rate of a single particle. During melting, $q_{i,rim}$ is reduced to maintain a constant rime mass fraction. The ice (rain) number sink (source) terms are proportional to the respective changes in $q_{i,ice}$: $N_{r,mlt} = Q_{r,mlt} N_{i,tot} / q_{i,ice}$. All remaining ice is transferred to the rain category when $F_{i,liq} > 0.99$.

M90 developed an equation for the melting behavior of an individual nonspherical unrimed ice crystal based on observations (Fujiyoshi 1986), using the thermodynamic

model of Mason (1956). Two processes control the melting rate. The first is latent heating (cooling) associated with condensation (evaporation) of water vapor at the particle's surface. The second is heat transfer from the environment to the particle surface and from the surface to the embedded ice core. During the melting process, it is assumed that the particle surface temperature is $T_0 = 273.15$ K. The change of ice-core mass from melting is

$$\left. \frac{dm_{\text{ice}}}{dt} \right|_{\text{melting}} = \frac{4\pi C(D_d, F_{i,\text{liq}}) F(D_d, F_{i,\text{liq}})}{L_f} \times [D_v \rho_a L_e (q_v - q_{s,0}) + k_a (T - T_0)], \quad (\text{A3})$$

where D_v is the diffusivity of water vapor in air, L_f (L_e) is the latent heat of fusion (evaporation), k_a is the thermal conductivity of air, q_v is the water vapor mass mixing ratio, $q_{s,0}$ is the saturated water vapor mass mixing ratio at the surface of the particle, $C(D_d, F_{i,\text{liq}})$ is the capacitance [appendix B; (B1)], and $F(D_d, F_{i,\text{liq}})$ is the ventilation coefficient [appendix B; (B2)]. The melting rate is treated in a simple way following most parameterizations (e.g., M90) that assumes the same ventilation coefficient and capacitance for both the latent term and the heat diffusion term in (A3).

b. Refreezing

The refreezing process describes how the liquid water surrounding the ice core freezes when mixed-phase particles are transported to regions where $T < 0^\circ\text{C}$. The refreezing source/sink term $Q_{l,\text{frz}}$ is

$$Q_{l,\text{frz}} = \int_0^\infty F_{i,\text{liq}} \left. \frac{dm_{\text{tot}}}{dt} \right|_{\text{freezing}} N_{0,p} D_p^{\mu_p} \exp(-\lambda_p D_p) dD_p, \quad (\text{A4})$$

where D_p is the full mixed-phase particle diameter and $F_{i,\text{liq}}[(dm_{\text{tot}}/dt)|_{\text{freezing}}]$ is the refreezing rate of a particle. The term $Q_{l,\text{frz}}$ represents a mass transfer from $q_{i,\text{liq}}$ to $q_{i,\text{rim}}$, and the rime density of refreezing ice is assumed to be near solid bulk ice (900 kg m^{-3}), following other drop freezing process in P3_ORIG.

From Pruppacher and Klett (1997), assuming a quasi-steady state during the refreezing process and a surface particle temperature of $T_0 = 273.15$ K, the freezing rate equation is a balance between the latent heat of freezing and the conduction through the ice shell formed around the whole particle. The conduction through the ice shell is given by the conduction of heat between the surrounding air and the particle and the heat exchange by evaporation/condensation at the particle surface:

$$\left. \frac{dm_{\text{tot}}}{dt} \right|_{\text{freezing}} = \frac{-4\pi C(D_p, F_{i,\text{liq}}) F(D_p, F_{i,\text{liq}})}{L_f} \times [D_v \rho_a L_s (q_v - q_{s,0}) + k_a (T - T_0)], \quad (\text{A5})$$

where L_s is the latent heat of sublimation, $C(D_p, F_{i,\text{liq}})$ is the capacitance [appendix B; (B7)], and $F(D_p, F_{i,\text{liq}})$ is the ventilation coefficient [appendix B; (B8)].

c. Collection with liquid-phase categories

It is assumed that rain $Q_{l,\text{coll},r}$ and cloud water $Q_{l,\text{coll},c}$ mass collected when $T \geq 0^\circ\text{C}$ is transferred into $q_{i,\text{liq}}$. At $T < 0^\circ\text{C}$ and in the dry growth regime, the collected rain and cloud masses are assumed to freeze instantaneously and are transferred to $q_{i,\text{rim}}$, as in P3_ORIG (MM15). At $T < 0^\circ\text{C}$ and in the wet growth regime, calculated following Musil (1970), the total collected rain and cloud mass $Q_{l,\text{wgrth}}$ is assumed to be a source for $q_{i,\text{liq}}$. Wet growth of hail is not the focus of the paper; however, prediction of $F_{i,\text{liq}}$ in P3_MOD presents an interesting possibility for improving the prediction of wet growth and shedding from hail.

The rain and cloud collection rates are parameterized using a collection kernel derived from the projected area and the terminal velocity relationships for rain and ice or mixed-phase particles, numerically integrated over the respective PSDs. The fall speed of cloud droplets is neglected in the kernel equation.

d. Vapor transfer

For simplicity, deposition/sublimation of ice in P3_MOD is allowed only when $F_{i,\text{liq}} = 0$ because liquid water is assumed to be distributed around the ice core when $F_{i,\text{liq}} > 0$. The calculation of deposition/sublimation follows from P3_ORIG (see MM15). Note that the $F_{i,\text{liq}}$ threshold for sublimation/deposition versus condensation/evaporation processes can be modified easily in P3_MOD. For example, it could be increased to 0.2 as in Thériault and Stewart (2010). If so, then the sublimation/deposition process would be calculated using the ice-core properties as for the melting process.

Vapor transfer of $q_{i,\text{liq}}$ (denoted $Q_{l,\text{dep}}$), which represents the liquid mass of mixed-phase particles lost by evaporation or gained by condensation, is also computed with the quasi-analytic formulation for supersaturation of MM15, using liquid-phase thermodynamic parameters. The $Q_{l,\text{dep}}$ source/sink term when $F_{i,\text{liq}} > 0$ is

$$Q_{l,\text{dep}} = \frac{A_{i,\text{wet}} \tau}{\tau_{i,\text{wet}} \Gamma_1} + (\delta_{t=0} - A_{i,\text{wet}} \tau) \frac{\tau}{\Delta t \tau_{i,\text{wet}} \Gamma_1} \times [1 - \exp(-\Delta t/\tau)], \quad (\text{A6})$$

where $\delta_{t=0}$ is the initial supersaturation, Δt is the time step, Γ_l the psychrometric correction associated with the latent heating/cooling, and $A_{i,\text{wet}}$ is the change in δ due to vertical motion, turbulent mixing,

and radiation. The overall supersaturation relaxation time scale in conditions when $F_{i,\text{liq}} > 0$ (τ) is $\tau^{-1} = \tau_c^{-1} + \tau_r^{-1} + \tau_{i,\text{wet}}^{-1}$. The supersaturation relaxation time scale associated with mixed-phase particles $\tau_{i,\text{wet}}$ is

$$\tau_{i,\text{wet}}^{-1} = \int_0^\infty 4\pi D_p \rho_a C(D_p, F_{i,\text{liq}}) F(D_p, F_{i,\text{liq}}) N_{0,p} D_p^{\mu_p} \exp(-\lambda_p D_p) dD_p, \quad (\text{A7})$$

where τ_c and τ_r are the relaxation time scales for cloud and rain, respectively (Morrison and Grabowski 2008), and $C(D_p, F_{i,\text{liq}})$ and $F(D_p, F_{i,\text{liq}})$ are the capacitance [appendix B; (B7)] and ventilation coefficient [appendix B; (B8)] relationships. During the evaporation process (when $Q_{l,\text{dep}} < 0$), which is computed gradually as a function of the liquid fraction, it is assumed that $N_{i,\text{tot}}$ decreases proportionally to the change in $q_{i,\text{tot}}$: $N_{l,\text{evp}} = Q_{l,\text{dep}} N_{i,\text{tot}} / q_{i,\text{tot}}$.

e. Shedding

Based on Rasmussen et al. (1984b), it is assumed that only ice particles with diameter larger than 9 mm within the PSD shed. The mass of $q_{i,\text{liq}}$ due to shedding $Q_{l,\text{shd}}$ is

given by the total integrated liquid mass of particles with $D_p > 9$ mm within the PSD and interpolating as a function of $F_{i,\text{rim}}$, with no shedding when $F_{i,\text{rim}} = 0$ and all liquid mass (for $D_p > 9$ mm) shed when $F_{i,\text{rim}} = 1$. The increase in the rain number mixing ratio from shedding assumes a mean raindrop diameter of 1 mm.

f. Sedimentation

The variables $q_{i,\text{liq}}$, $q_{i,\text{tot}}$, $q_{i,\text{rim}}$, and $B_{i,\text{rim}}$ use the total mass-weighted fall speed V_m for their sedimentation, while the number mixing ratio $N_{i,\text{tot}}$ uses the number-weighted fall speed V_N , given by, respectively,

$$V_m = \frac{\int_0^\infty V_t(D_p, F_{i,\text{liq}}) m_t(D_p, F_{i,\text{liq}}) N_{0,p} D_p^{\mu_p} \exp(-\lambda_p D_p) dD_p}{\int_0^\infty m_t(D_p, F_{i,\text{liq}}) N_{0,p} D_p^{\mu_p} \exp(-\lambda_p D_p) dD_p}, \quad (\text{A8})$$

$$V_N = \frac{\int_0^\infty V_t(D_p, F_{i,\text{liq}}) N_{0,p} D_p^{\mu_p} \exp(-\lambda_p D_p) dD_p}{\int_0^\infty N_{0,p} D_p^{\mu_p} \exp(-\lambda_p D_p) dD_p}, \quad (\text{A9})$$

where $V_t(D_p, F_{i,\text{liq}})$ is given by (13) in section 3b. An increase of both V_m and V_N occurs with increasing $F_{i,\text{liq}}$ in P3_MOD (see Fig. 1).

All integrations are done offline, and the values are stored in lookup tables as a function of 50 values of normalized total ice mass $q_{i,\text{tot}}/N_{i,\text{tot}}$, five bulk rime densities $\rho_{i,\text{rim}}$ (50, 250, 450, 650, and 900 kg m⁻³), four bulk rime mass fractions $F_{i,\text{rim}}$ (0, 0.333, 0.667, and 1), and four bulk liquid mass fractions $F_{i,\text{liq}}$ (0, 0.333, 0.667, and 1).

APPENDIX B

Capitance and Ventilation Coefficient

a. Processes depending on the ice-core properties

The capacitance $C(D_d, F_{i,\text{liq}})$ accounts for non-spherical shape of ice particles undergoing melting or

deposition/sublimation. The capacitance is calculated simply by a linear interpolation based on $F_{i,\text{liq}}$ between the capacitance of an ice particle $C_d(D_d)$ when $F_{i,\text{liq}} = 0$ and that of a spherical drop $C_{\text{liq}}(D_d) = 0.5D_d$ when $F_{i,\text{liq}} = 1$, for a given D_d :

$$C(D_d, F_{i,\text{liq}}) = (1 - F_{i,\text{liq}})C_d(D_d) + F_{i,\text{liq}}C_{\text{liq}}(D_d), \quad (\text{B1})$$

where $C_d(D_d)$ is a function of the ice particle properties for each regime of the distribution as detailed in MM15.

The ventilation coefficient $F(D_d, F_{i,\text{liq}})$ for the melting calculation is also given by linear interpolation over $F_{i,\text{liq}}$ between the value for an ice particle $F_d(D_d)$ when $F_{i,\text{liq}} = 0$ from P3_ORIG and that of a liquid drop $F_{\text{liq}}(D_d)$ when $F_{i,\text{liq}} = 1$:

$$F(D_d, F_{i,\text{liq}}) = (1 - F_{i,\text{liq}})F_d(D_d) + F_{i,\text{liq}}F_{\text{liq}}(D_d), \quad (\text{B2})$$

where $F_d(D_d)$ is (Thorpe and Mason 1966)

$$F_d(D_d) = \begin{cases} 1 & \text{if } D_d < 100 \mu\text{m} \\ 0.65 + 0.44X_d & \text{if } D_d \geq 100 \mu\text{m} \end{cases} \quad (\text{B3})$$

and $X_d = \text{Sc}^{1/3} \text{Re}_d^{1/2}$, $\text{Re}_d = V_t(D_d, F_{i,\text{liq}} = 0) D_d \rho_a / \nu$ is the Reynolds number, ν is the dynamic viscosity of air, and Sc is the Schmidt number $\text{Sc} = \nu / (\rho_a D_v)$. The terminal velocity $V_t(D_d, F_{i,\text{liq}} = 0)$ follows Mitchell and Heymsfield (2005) with $F_{i,\text{liq}} = 0$, as in P3_ORIG:

$$V_t(D_d, F_{i,\text{liq}} = 0) = a_1 v^{1-2b_1} \left(\frac{2g}{\rho_a} \right)^{b_1} \left[\frac{m_d(D_d)}{A_d(D_d)} \right]^{b_1} D_d^{2b_1-1}, \quad (\text{B4})$$

$$a_1 = c_2 (1 + c_1 X^{1/2})^{1/2} - 1 / (X^{b_1}), \quad (\text{B4a})$$

$$b_1 = c_2 X^{1/2} / \{2[(1 + c_1 X^{1/2})^{1/2} - 1](1 + c_1 X^{1/2})^{1/2}\}, \quad (\text{B4b})$$

$$c_1 = 4 / (5.83^2 \times 0.6^{1/2}), \quad (\text{B4c})$$

$$c_2 = 5.83^2 / 4, \quad (\text{B4d})$$

$$X = 2g\rho_a / (\nu\rho_a) [m_d(D_d) / A_d(D_d)]^{b_1} D_d^{2b_1-1}. \quad (\text{B4e})$$

The term $F_{\text{liq}}(D_d)$ is (Pruppacher and Klett 1997)

$$F_{\text{liq}}(D_d) = \begin{cases} 1 & \text{if } D_d < 100 \mu\text{m} \\ 0.78 + 0.28 X_r & \text{if } D_d \geq 100 \mu\text{m} \end{cases}, \quad (\text{B5})$$

with $X_r = \text{Sc}^{1/3} \text{Re}_r^{1/2}$, $\text{Re}_r = V_t(D_d, F_{i,\text{liq}} = 1) D_d \rho_a / \nu$. The $V_t(D_d, F_{i,\text{liq}} = 1)$ is the terminal velocity for $F_{i,\text{liq}} = 1$ and is computed using Simmel et al. (2002), Beard (1976), and Gunn and Kinzer (1949):

$$V_t(D_d, F_{i,\text{liq}} = 1) = \begin{cases} 4579.4 \text{ m}^{2/3} & \text{if } D_d \leq 134.43 \mu\text{m} \\ 49.62 \text{ m}^{1/3} & \text{if } D_d < 1511.64 \mu\text{m} \\ 17.32 \text{ m}^{1/6} & \text{if } D_d < 3477.84 \mu\text{m} \\ 9.17 & \text{if } D_d < 3477.84 \mu\text{m} \end{cases}, \quad (\text{B6})$$

where $m = \pi/6 \rho_{w,g} D_d^3$ and $\rho_{w,g} = 1 \text{ g m}^{-3}$ is the density of water.

Equations (B1) and (B2) are the formulations to express the capacitance and ventilation coefficient as a function of the ice-core diameter, in contrast to those used in M90 that also depend on the real particle diameter. Although the capacitance and ventilation coefficient used for the latent heat term in the melting (A3) should also depend on the liquid part of the particle, the melting equation is treated following most parameterizations (e.g., Milbrandt and Yau 2005; M90) that assume the same ventilation coefficient and capacitance for both the latent heat term and the heat diffusion term in (A3). Note also that the relationships for capacitance and ventilation coefficient differ for $F_{i,\text{liq}} = 0$ between M90

and P3 and the M90 coefficients are only for unrimed particles, which is why we use the P3 coefficients rather than M90.

b. Processes depending on properties of the entire particle

For condensation/evaporation and refreezing of mixed-phase particles with $F_{i,\text{liq}} > 0$, the capacitance $C(D_p, F_{i,\text{liq}})$ is similar to (B1) but uses the full particle diameter D_p :

$$C(D_p, F_{i,\text{liq}}) = (1 - F_{i,\text{liq}}) C_d(D_p) + F_{i,\text{liq}} C_{\text{liq}}(D_p). \quad (\text{B7})$$

The ventilation coefficient $F(D_p, F_{i,\text{liq}})$ is (Thorpe and Mason 1966)

$$F(D_p, F_{i,\text{liq}}) = \begin{cases} 1 & \text{if } D_p < 100 \mu\text{m} \\ 0.65 + 0.44 X_p & \text{if } D_p \geq 100 \mu\text{m} \end{cases}, \quad (\text{B8})$$

where $X_p = \text{Sc}^{1/3} \text{Re}^{1/2}$, $\text{Re} = V_t(D_p, F_{i,\text{liq}}) D_p \rho_a / \nu$, and $V_t(D_p, F_{i,\text{liq}})$ is given by (13), which uses D_p instead of D_d in (B4) to (B6).

REFERENCES

- Austin, P. M., and A. C. Bemis, 1950: A quantitative study of the "bright band" in radar precipitation echoes. *J. Meteor.*, **7**, 145–151, [https://doi.org/10.1175/1520-0469\(1950\)007<0145:AQSTB>2.0.CO;2](https://doi.org/10.1175/1520-0469(1950)007<0145:AQSTB>2.0.CO;2).
- Barszcz, A., 2017: Impacts du gel par collision sur la production de pluie verglaçante. M.S. thesis, Dépt. des Sciences de la Terre et de l'Atmosphère, Université du Québec à Montréal, 89 pp.
- , J. A. Milbrandt, and J. M. Thériault, 2018: Improving the explicit prediction of freezing rain in a kilometer-scale numerical weather prediction model. *Wea. Forecasting*, **33**, 767–782, <https://doi.org/10.1175/WAF-D-17-0136.1>.
- Beard, K. V., 1976: Terminal velocity and shape of cloud and precipitation drops aloft. *J. Atmos. Sci.*, **33**, 851–864, [https://doi.org/10.1175/1520-0469\(1976\)033<0851:TVASOC>2.0.CO;2](https://doi.org/10.1175/1520-0469(1976)033<0851:TVASOC>2.0.CO;2).
- Braun, S. A., and R. A. Houze Jr., 1995: Melting and freezing in a mesoscale convective system. *Quart. J. Roy. Meteor. Soc.*, **121**, 55–77, <https://doi.org/10.1002/qj.49712152104>.
- Brown, P. R. A., and P. N. Francis, 1995: Improved measurements of the ice water content in cirrus using a total-water probe. *J. Atmos. Oceanic Technol.*, **12**, 410–414, [https://doi.org/10.1175/1520-0426\(1995\)012<0410:IMOTIW>2.0.CO;2](https://doi.org/10.1175/1520-0426(1995)012<0410:IMOTIW>2.0.CO;2).
- Carmichael, H. E., R. E. Stewart, W. Henson, and J. M. Thériault, 2011: Environmental conditions favoring ice pellet aggregation. *Atmos. Res.*, **101**, 844–851, <https://doi.org/10.1016/j.atmosres.2011.05.015>.
- Dietlicher, R., D. Neubauer, and U. Lohmann, 2018: Prognostic parameterization of cloud ice with a single category in the aerosol-climate model ECHAM (v6.3.0)-HAM (v2.3). *Geosci. Model Dev.*, **11**, 1557–1576, <https://doi.org/10.5194/gmd-11-1557-2018>.
- Doms, G., and U. Schättler, 2002: A description of the non-hydrostatic regional model LM—Part I: Dynamics and numerics. Deutscher Wetterdienst Tech. Rep., 134 pp.

- Fabry, F., and I. Zawadzki, 1995: Long-term radar observations of the melting layer of precipitation and their interpretation. *J. Atmos. Sci.*, **52**, 838–851, [https://doi.org/10.1175/1520-0469\(1995\)052<0838:LTR00T>2.0.CO;2](https://doi.org/10.1175/1520-0469(1995)052<0838:LTR00T>2.0.CO;2).
- , and W. Szyrmer, 1999: Modeling of the melting layer. Part II: Electromagnetic. *J. Atmos. Sci.*, **56**, 3593–3600, [https://doi.org/10.1175/1520-0469\(1999\)056<3593:MOTMLP>2.0.CO;2](https://doi.org/10.1175/1520-0469(1999)056<3593:MOTMLP>2.0.CO;2).
- Frick, C., A. Seifert, and H. Wernli, 2013: A bulk parameterization of melting snowflakes with explicit liquid water fraction for the COSMO model. *Geosci. Model Dev.*, **6**, 1925–1939, <https://doi.org/10.5194/gmd-6-1925-2013>.
- Fujiyoshi, Y., 1986: Melting snowflakes. *J. Atmos. Sci.*, **43**, 307–311, [https://doi.org/10.1175/1520-0469\(1986\)043<0307:MS>2.0.CO;2](https://doi.org/10.1175/1520-0469(1986)043<0307:MS>2.0.CO;2).
- Geresdi, I., N. Sarkadi, and G. Thompson, 2014: Effect of the accretion by water drops on the melting of snowflakes. *Atmos. Res.*, **149**, 96–110, <https://doi.org/10.1016/j.atmosres.2014.06.001>.
- Gibson, S. R., and R. E. Stewart, 2007: Observations of ice pellets during a winter storm. *Atmos. Res.*, **85**, 64–76, <https://doi.org/10.1016/j.atmosres.2006.11.004>.
- Gunn, R., and D. G. Kinzer, 1949: The terminal velocity of fall for water droplets in stagnant air. *J. Meteor.*, **6**, 243–248, [https://doi.org/10.1175/1520-0469\(1949\)006<0243:TTVOFF>2.0.CO;2](https://doi.org/10.1175/1520-0469(1949)006<0243:TTVOFF>2.0.CO;2).
- Gyakum, J. R., and P. J. Roebber, 2001: The 1998 ice storm—Analysis of a planetary-scale event. *Mon. Wea. Rev.*, **129**, 2983–2997, [https://doi.org/10.1175/1520-0493\(2001\)129<2983:TISAOA>2.0.CO;2](https://doi.org/10.1175/1520-0493(2001)129<2983:TISAOA>2.0.CO;2).
- Hanesiak, J. M., and R. E. Stewart, 1995: The mesoscale and microscale structure of a severe ice pellet storm. *Mon. Wea. Rev.*, **123**, 3144–3162, [https://doi.org/10.1175/1520-0493\(1995\)123<3144:TMAMSO>2.0.CO;2](https://doi.org/10.1175/1520-0493(1995)123<3144:TMAMSO>2.0.CO;2).
- Heymsfield, A. J., 2003: Properties of tropical and midlatitude ice cloud particle ensembles. Part II: Applications for mesoscale and climate models. *J. Atmos. Sci.*, **60**, 2592–2611, [https://doi.org/10.1175/1520-0469\(2003\)060<2592:POTAMI>2.0.CO;2](https://doi.org/10.1175/1520-0469(2003)060<2592:POTAMI>2.0.CO;2).
- Hogan, A. W., 1985: Is sleet a contact nucleation phenomenon? *Proc. 42nd Eastern Snow Conf.*, Montreal, Quebec, Eastern Snow Conference, 292–294.
- Hogan, R. J., L. Tian, P. R. A. Brown, C. D. Westbrook, A. J. Heymsfield, and J. D. Eastment, 2012: Radar scattering from ice aggregates using the horizontally aligned oblate spheroid approximation. *J. Appl. Meteor. Climatol.*, **51**, 655–671, <https://doi.org/10.1175/JAMC-D-11-074.1>.
- Isaac, G. A., and Coauthors, 2014: Science of Nowcasting Olympic Weather for Vancouver 2010 (SNOW-V10): A World Weather Research Programme project. *Pure Appl. Geophys.*, **171**, 1–24, <https://doi.org/10.1007/s00024-012-0579-0>.
- Lackmann, G. M., K. Keeter, L. G. Lee, and M. B. Ek, 2002: Model representation of freezing and melting precipitation: Implications for winter weather forecasting. *Wea. Forecasting*, **17**, 1016–1033, [https://doi.org/10.1175/1520-0434\(2003\)017<1016:MROFAM>2.0.CO;2](https://doi.org/10.1175/1520-0434(2003)017<1016:MROFAM>2.0.CO;2).
- Leinonen, J., and A. von Lerber, 2018: Snowflake melting simulation using smoothed particle hydrodynamics. *J. Geophys. Res. Atmos.*, **123**, 1811–1825, <https://doi.org/10.1002/2017JD027909>.
- Lin, C. A., and R. E. Stewart, 1986: Mesoscale circulations initiated by melting snow. *J. Geophys. Res.*, **91**, 13 299–13 302, <https://doi.org/10.1029/JD091iD12p13299>.
- Mason, B. J., 1956: On the melting of hailstones. *Quart. J. Roy. Meteor. Soc.*, **82**, 209–216, <https://doi.org/10.1002/qj.49708235207>.
- Matsuo, T., and Y. Sayso, 1981: Melting of snowflakes below freezing level in the atmosphere. *J. Meteor. Soc. Japan*, **59**, 10–25, https://doi.org/10.2151/jmsj1965.59.1_10.
- Milbrandt, J. A., and M. K. Yau, 2005: A multimoment bulk microphysics parameterization. Part I: Analysis of the role of the spectral shape parameter. *J. Atmos. Sci.*, **62**, 3051–3064, <https://doi.org/10.1175/JAS3534.1>.
- , and H. Morrison, 2016: Parameterization of cloud microphysics based on the prediction of bulk ice particle properties. Part III: Introduction of multiple free categories. *J. Atmos. Sci.*, **73**, 975–995, <https://doi.org/10.1175/JAS-D-15-0204.1>.
- Mitchell, D. L., and A. J. Heymsfield, 2005: The treatment of ice particle terminal velocities, highlighting aggregates. *J. Atmos. Sci.*, **62**, 1637–1644, <https://doi.org/10.1175/JAS3413.1>.
- Mitra, S. K., O. Vohl, M. Ahr, and H. R. Pruppacher, 1990: A wind tunnel and theoretical study of the melting behavior of atmospheric ice particles. Part IV: Experiment and theory for snowflakes. *J. Atmos. Sci.*, **47**, 584–591, [https://doi.org/10.1175/1520-0469\(1990\)047<0584:AWTATS>2.0.CO;2](https://doi.org/10.1175/1520-0469(1990)047<0584:AWTATS>2.0.CO;2).
- Morrison, H., and W. W. Grabowski, 2008: Modeling supersaturation and subgrid-scale mixing with two-moment bulk warm microphysics. *J. Atmos. Sci.*, **65**, 792–812, <https://doi.org/10.1175/2007JAS2374.1>.
- , and J. A. Milbrandt, 2015: Parameterization of cloud microphysics based on the prediction of the bulk ice particle properties. Part I: Scheme description and idealized tests. *J. Atmos. Sci.*, **72**, 287–311, <https://doi.org/10.1175/JAS-D-14-0065.1>.
- , G. Thompson, and V. Tatarskii, 2009: Impact of cloud microphysics on the development of trailing stratiform precipitation in a simulated squall line: Comparison of one- and two-moment schemes. *Mon. Wea. Rev.*, **137**, 991–1007, <https://doi.org/10.1175/2008MWR2556.1>.
- Musil, D. J., 1970: Computer modeling of hailstone growth in feeder clouds. *J. Atmos. Sci.*, **27**, 474–482, [https://doi.org/10.1175/1520-0469\(1970\)027<0474:CMOHGI>2.0.CO;2](https://doi.org/10.1175/1520-0469(1970)027<0474:CMOHGI>2.0.CO;2).
- Phillips, V. T. J., A. Pokrovsky, and A. Khain, 2007: The influence of time-dependent melting on the dynamics and precipitation production in maritime and continental storm clouds. *J. Atmos. Sci.*, **64**, 338–359, <https://doi.org/10.1175/JAS3832.1>.
- , A. Khain, N. Benmoshe, and E. Ilotoviz, 2014: Theory of time-dependent freezing. Part I: Description of scheme for wet growth of hail. *J. Atmos. Sci.*, **71**, 4527–4557, <https://doi.org/10.1175/JAS-D-13-0375.1>.
- Pruppacher, H. R., and J. D. Klett, 1997: *Microphysics of Clouds and Precipitation*. Atmospheric and Oceanographic Sciences Library, Vol. 18, Springer, 954 pp.
- Rasmussen, R., and H. R. Pruppacher, 1982: A wind tunnel and theoretical study of the melting behavior of atmospheric ice particles. Part I: A wind tunnel study of frozen drops of radius < 500 μm . *J. Atmos. Sci.*, **39**, 152–158, [https://doi.org/10.1175/1520-0469\(1982\)039<0152:AWTATS>2.0.CO;2](https://doi.org/10.1175/1520-0469(1982)039<0152:AWTATS>2.0.CO;2).
- , V. Levizzani, and H. R. Pruppacher, 1984a: A wind tunnel and theoretical study of the melting behavior of atmospheric ice particles. Part II: A theoretical study for frozen drops of radius < 500 μm . *J. Atmos. Sci.*, **41**, 374–380, [https://doi.org/10.1175/1520-0469\(1984\)041<0374:AWTATS>2.0.CO;2](https://doi.org/10.1175/1520-0469(1984)041<0374:AWTATS>2.0.CO;2).
- , —, and —, 1984b: A wind tunnel and theoretical study of the melting behavior of atmospheric ice particles. Part III: Experiment and theory for spherical ice particles of radius > 500 μm . *J. Atmos. Sci.*, **41**, 381–388, [https://doi.org/10.1175/1520-0469\(1984\)041<0381:AWTATS>2.0.CO;2](https://doi.org/10.1175/1520-0469(1984)041<0381:AWTATS>2.0.CO;2).
- Reeves, H. D., A. V. Ryzhkov, and J. Krause, 2016: Discrimination between winter precipitation types based on spectral-bin microphysical modeling. *J. Appl. Meteor. Climatol.*, **55**, 1747–1761, <https://doi.org/10.1175/JAMC-D-16-0044.1>.

- Simmel, M., T. Trautmann, and G. Tetzlaff, 2002: Numerical solution of the stochastic collection equation—Comparison of the linear discrete method with other methods. *Atmos. Res.*, **61**, 135–148, [https://doi.org/10.1016/S0169-8095\(01\)00131-4](https://doi.org/10.1016/S0169-8095(01)00131-4).
- Stewart, R. E., 1985: Precipitation types in winter storms. *Pure Appl. Geophys.*, **123**, 597–609, <https://doi.org/10.1007/BF00877456>.
- Szyrmer, W., and I. Zawadzki, 1999: Modeling of the melting layer. Part I: Dynamics and microphysics. *J. Atmos. Sci.*, **56**, 3573–3592, [https://doi.org/10.1175/1520-0469\(1999\)056<3573:MOTMLP>2.0.CO;2](https://doi.org/10.1175/1520-0469(1999)056<3573:MOTMLP>2.0.CO;2).
- Thériault, J. M., and R. E. Stewart, 2010: A parameterization of the microphysical processes forming many types of winter precipitation. *J. Atmos. Sci.*, **67**, 1492–1508, <https://doi.org/10.1175/2009JAS3224.1>.
- , —, J. A. Milbrandt, and M. K. Yau, 2006: On the simulation of winter precipitation types. *J. Geophys. Res.*, **111**, D18202, <https://doi.org/10.1029/2005JD006665>.
- , —, and W. Henson, 2010: On the dependence of winter precipitation types on temperature, precipitation rate, and associated features. *J. Appl. Meteor. Climatol.*, **49**, 1429–1442, <https://doi.org/10.1175/2010JAMC2321.1>.
- , K. L. Rasmussen, T. Fisco, R. E. Stewart, P. Joe, I. Gultepe, M. Clément, and G. A. Isaac, 2014: Weather observations along Whistler Mountain in five storms during SNOW-V10. *Pure Appl. Geophys.*, **171**, 129–155, <https://doi.org/10.1007/s00024-012-0590-5>.
- Thompson, G., P. R. Field, R. M. Rasmussen, and W. D. Hall, 2008: Explicit forecasts of winter precipitation using an improved bulk microphysics scheme. Part II: Implementation of a new snow parameterization. *Mon. Wea. Rev.*, **136**, 5095–5115, <https://doi.org/10.1175/2008MWR2387.1>.
- Thorpe, A. D., and B. J. Mason, 1966: The evaporation of ice spheres and ice crystals. *Br. J. Appl. Phys.*, **17**, 541–548, <https://doi.org/10.1088/0508-3443/17/4/316>.
- Walko, R. L., W. R. Cotton, G. Feingold, and B. Stevens, 2000: Efficient computation of vapor and heat diffusion between hydrometeors in a numerical model. *Atmos. Res.*, **53**, 171–183, [https://doi.org/10.1016/S0169-8095\(99\)00044-7](https://doi.org/10.1016/S0169-8095(99)00044-7).
- Yokoyama, T., and H. Tanaka, 1984: Microphysical processes of melting snowflakes detected by two-wavelength radar—Part I: Principle of measurement based on model calculation. *J. Meteor. Soc. Japan*, **62**, 650–667, https://doi.org/10.2151/jmsj1965.62.4_650.